
**AFRL-AFOSR-VA-TR-2023-0436**

# Crossed-Field Device Physics in Perturbed Systems

**Browning, Jim**
**BOISE STATE UNIVERSITY**
**1910 UNIVERSITY DR**
**BOISE, ID, 83725**
**USA**

**08/24/2023**
**Final Technical Report**



Air Force Research Laboratory
Air Force Office of Scientific Research
Arlington, Virginia 22203
Air Force Materiel Command

# REPORT DOCUMENTATION PAGE

**PLEASE DO NOT RETURN YOUR FORM TO THE ABOVE ORGANIZATION.**

| 1. REPORT DATE | 2. REPORT TYPE | 3. DATES COVERED | |
|---|---|---|---|
| 20230824 | Final | START DATE<br>20190415 | END DATE<br>20230414 |

**4. TITLE AND SUBTITLE**
Crossed-Field Device Physics in Perturbed Systems

| 5a. CONTRACT NUMBER | 5b. GRANT NUMBER | 5c. PROGRAM ELEMENT NUMBER |
|---|---|---|
| | FA9550-19-1-0101 | 61102F |
| **5d. PROJECT NUMBER** | **5e. TASK NUMBER** | **5f. WORK UNIT NUMBER** |
| | | |

**6. AUTHOR(S)**
Jim Browning

**7. PERFORMING ORGANIZATION NAME(S) AND ADDRESS(ES)**
BOISE STATE UNIVERSITY
1910 UNIVERSITY DR
BOISE, ID 83725
USA

**8. PERFORMING ORGANIZATION REPORT NUMBER**

| 9. SPONSORING/MONITORING AGENCY NAME(S) AND ADDRESS(ES) | 10. SPONSOR/MONITOR'S ACRONYM(S) | 11. SPONSOR/MONITOR'S REPORT NUMBER(S) |
|---|---|---|
| Air Force Office of Scientific Research<br>875 N. Randolph St. Room 3112<br>Arlington, VA 22203 | AFRL/AFOSR RTB1 | AFRL-AFOSR-VA-TR-2023-0436 |

**12. DISTRIBUTION/AVAILABILITY STATEMENT**
A Distribution Unlimited: PB Public Release

**13. SUPPLEMENTARY NOTES**

**14. ABSTRACT**
The project consists of theoretical, simulation, and experimental studies of electron stability and interactions in simple crossed-field systems and in magnetrons. Simulation results in planar crossed-field configurations demonstrate electron stability thresholds in current density and magnetic field tilt that agree with 1D theory and have been compared to experimental results. These experiments agree well with theory and simulation and utilized gated field emitters arrays as the electron sources. The experimental efforts have begun advancing as new gated field emitter arrays have been fabricated and are being tested. Eight devices have demonstrated > 40 mA of current at 60 V pulsed and were used in the experiments. Magnetron simulations in 2D and 3D (industrial magnetron) have been analyzed using two newly developed electron population techniques: intensity plots and breadth ratio. These new techniques show that prior to oscillation there is a dip in the azimuthal velocity distribution indicating highly cycloidal electrons near the cathode. To study the startup physics, electrons were injected in a counter rotation direction to purposely create highly cycloidal electrons. These simulations show much faster startup of the magnetron indicating that the “dip” in the azimuthal breadth ratio may show an electron population condition leading to startup. In other simulations, a cylindrical smooth anode geometry was used to study the transition to Brillouin flow by turning electron injection off and watching the azimuthal breadth ratio change versus time as it should go to infinity for purely laminar flow.

**15. SUBJECT TERMS**

| 16. SECURITY CLASSIFICATION OF: | | | 17. LIMITATION OF ABSTRACT | 18. NUMBER OF PAGES |
|---|---|---|---|---|
| a. REPORT | b. ABSTRACT | c. THIS PAGE | | |
| U | U | U | UU | 61 |

| 19a. NAME OF RESPONSIBLE PERSON | 19b. PHONE NUMBER *(Include area code)* |
|---|---|
| JOHN LUGINSLAND | 000-0000 |

**Standard Form 298** (Rev.5/2020)
Prescribed by ANSI Std. Z39.18

# Crossed-Field Device Physics in Perturbed Systems

FA9550-19-1-0101

Final Report, July 13, 2023

Ranajoy Bhattacharya and Jim Browning

Boise State University, Boise, ID

Adam Darr and Allen Garner

Purdue University, West Lafayette, IN

Winston Chern and Akintunde I. Akinwande

Massachusetts Institute of Technology, Cambridge MA.

## ABSTRACT

The project consists of theoretical, simulation, and experimental studies of electron stability and interactions in simple crossed-field systems and in magnetrons. Simulation results in planar crossed-field configurations demonstrate electron stability thresholds in current density and magnetic field tilt that agree with 1D theory and have been compared to experimental results. These experiments agree well with theory and simulation and utilized gated field emitters arrays as the electron sources. The experimental efforts have begun advancing as new gated field emitter arrays have been fabricated and are being tested. Eight devices have demonstrated > 40 mA of current at 60 V pulsed and were used in the experiments. Magnetron simulations in 2D and 3D (industrial magnetron) have been analyzed using two newly developed electron population techniques: intensity plots and breadth ratio. These new techniques show that prior to oscillation there is a dip in the azimuthal velocity distribution indicating highly cycloidal electrons near the cathode. To study the startup physics, electrons were injected in a counter rotation direction to purposely create highly cycloidal electrons. These simulations show much faster startup of the magnetron indicating that the “dip” in the azimuthal breadth ratio may show an electron population condition leading to startup. In other simulations, a cylindrical smooth anode geometry was used to study the transition to Brillouin flow by turning electron injection off and watching the azimuthal breadth ratio change versus time as it should go to infinity for purely laminar flow.

# Chapter I. Introduction

Our research goal is to study crossed-field device physics with convergence of theory, simulation, and experiment to understand these systems during various perturbations. Here, we show the study of four crossed-field configurations: *simple planar, simple cylindrical, magnetron, and Crossed-field amplifier (CFA)*. Hence, we move from the study of simple devices to more complicated devices. The theoretical development will look first at the simple geometries moving from planar to cylindrical. We use simulations, such as CST for particle trajectory modeling and the particle-in-cell (PIC) code Vsim, to study magnetrons and CFAs. We have developed a VSim magnetron model based on the L3-Harris Technologies CWM-75KW magnetron. To study crossed-field devices experimentally, MIT is fabricating Gated Field Emission Arrays (GFEAs) to use in our Crossed-Field system and our magnetron experiment. Hence, this project includes theory, simulation, and experiment. The perturbed systems include: *AC modulation of the anode to cathode voltage, tilted magnetic field with magnetic field component in the anode to cathode direction, and electron modulation with a continuous current background or for magnetron control.* These perturbed system studies are shown in Table 1. The program objectives include improving the understanding of basic device physics in crossed-field systems; comparing theory, simulation, and experiment in multiple configurations to ensure the results are consistent across geometries; and studying the effects of perturbations, including electron modulation, on these systems to improve device performance and expand applications. This report is broken down by research groups: Boise State University (BSU), Purdue University, and the Massachusetts Institute of Technology (MIT)

***Table 1. Perturbed system research studies***

| **Perturbation Study** | **Approach** | **Type of Study** |
|---|---|---|
| AC Modulation of Anode to Cathode Voltage | Low frequency ($<\omega_c$ ) modulation of cathode voltage (1% of $V_{DC}$ ) | Theory, simulation, experiment in planar and cylindrical geometries |
| Tilted magnetic field | Apply magnetic field component along anode-cathode direction | Theory, simulation, experiment in planar and cylindrical geometries |
| Modulated electrons in hub | Combine modulation and continuous injection current to study hub stability and noise propagation | Theory, simulation, experiment in simple planar and cylindrical geometries |
| Modulated electrons in magnetron | Modulate electrons at operating frequency to control start-up and phase and study noise by modulating phase and power during oscillation | Simulation and experimental magnetron system to look at the effects of phase and power modulation |
| Modulated electrons in CFA | Modulate electrons at operating frequency to study gain, bandwidth, and noise | Simulation only |

# Chapter II. Simulation of a Planar Crossed-Field Device (BSU).

## Introduction

A simple, planar crossed field system of 10 cm wide and 20 cm long with a variable gap of 0.5 cm to 2 cm had been studied through simulation and a CAD model based on the simulation was developed for experiment. The simulation model and initial results was discussed in the prior year report. Mainly, three parameters were studied using simulation which is also benchmarked using experiment and theory. Experimental parameters are given in Table II.1. The anode-cathode distance is varied along with the strength and tilt of the magnetic field.

| Parameters | Value | Type of Study |
|---|---|---|
| Anode-Cathode distance | 5 mm to 20 mm | Theory, simulation, experiment in planar geometries |
| Magnetic field | 0.01 T to 0.05 T | Theory, simulation, experiment in planar geometries |
| Driving voltage | 3kV | Theory, simulation, experiment in simple planar geometries |
| Effect of tilted magnetic field | $0^o$ to $5^o$ | Simulation, experiment in simple planar geometries |

*Table II.1: Planar Crossed-Field Studies*

## CF Simulation

The simulation was carried using a simple space charge limited emission model with a fixed current of 1.5 mA in CST. The sole electrode was kept at -3000V while the electron source emitter was kept at +200 V relative to the anode (-2800 V). Anode is fixed at ground. The anode-cathode distance was varied from 5 mm to 20 mm. Two models, with and without axial end-hats, were used to analyze beam spreading. From Figure II.1 it is clear that the end-hats are necessary to confine the beam axially as the simulations using CST show the highly cycloidal beams. Magnetic field strength was varied from 0.01 T to 0.05 T with a step size of 0.01 T to look beam stability condition. Primarily two parameters were studied.

(a) Effect of current density

(b) Effect of tilted magnetic field

The results were well matching with the theory and was demonstrated in first year.

# Chapter III. Design and Fabrication of Experimental Crossed-Field System (BSU and MIT)

A. Preparation of experimental setup

In this project, two different test chambers are being used for the experiments. A crossed-field experiment chamber and another test chamber for silicon gated field emitter array (GFEA) characterization. Details of those chambers and test equipment were described in previous year report. In summary, a planar test jig was fabricated and shown in Fig. III.1. The crossed-field structure is fabricated with the segmented collector and anode. The cathode (sole) electrode is aluminum. This assembly consists of Low temperature co-fired ceramic (LTCC) structures to form the segmented anode, end collector, end-hats, and GFEA connector as shown in Figure III.1. In this configuration, an "injected beam" configuration is being used based on the Gated field emitter array (GFEA) provided by MIT. Mounted GFEAs can be seen at the bottom of the Figure. III.1. The details of the experimental setup were described in previous year report.

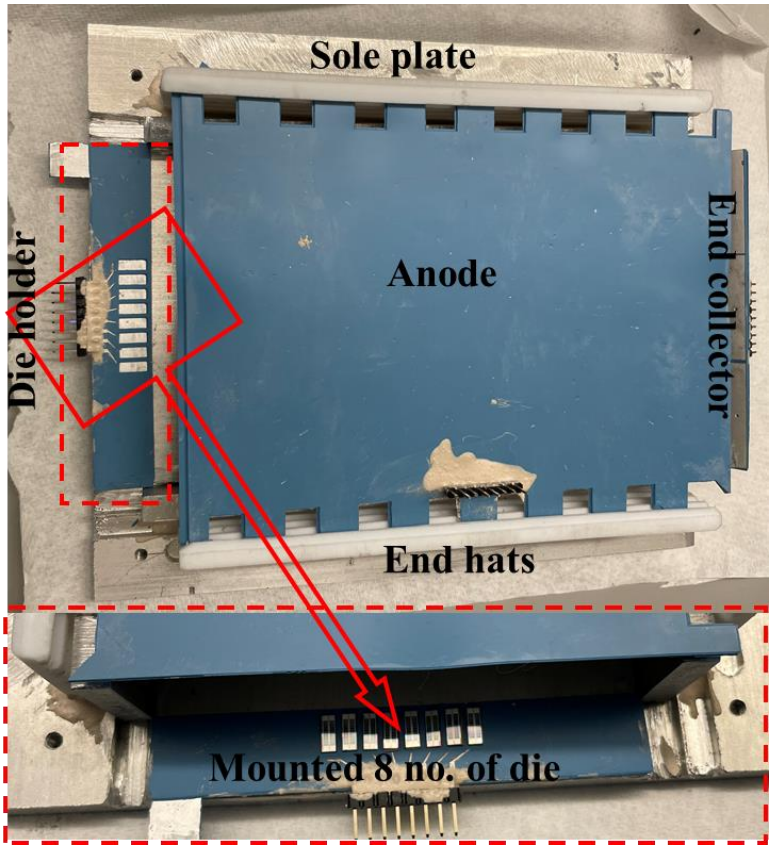


Figure III.1: Assembled dummy test jig. The test jig consists of an anode, sole, end hats, end collector and GFEA holder. 8 GFEA's can be seen mounted in the holder.

An existing test chamber were used to test the GFEA die before use in the CF or magnetron experiments. The details of the test chamber and experimental setup were described in previous year report.

B. Experimental characterization of gated field emitter array

The GFEA die from MIT were tested before those were mounted in the planar test jig. Figure III.2 shows the I-V characteristics of one of the die under test. The die has a collector current of 2.4 mA with a gate leakage current of 61µA. The primary goal of these characterization study was to find die with higher emission current (> 5 mA per die) and store them for the cross-field device and magnetron experiments. Figure III.3 shows a die with collector current of 5.27 mA and a gate leakage current of 1.02 mA (Figure III.13). However, after the UV exposure of 100 minute the collector current improved by 10 times (≈ 54.24 mA) and the gate leakage current reduced by 3 times (Figure. III 3). UV exposure [4] helps to remove desorb residuals gases, such as water vapor, from emitter tip surfaces and also from dielectric walls between emitter and gate. Removal of adsorbates helps in reducing the work function of emitters and reducing the leakage path in dielectric, thus, improving the overall field emission current.

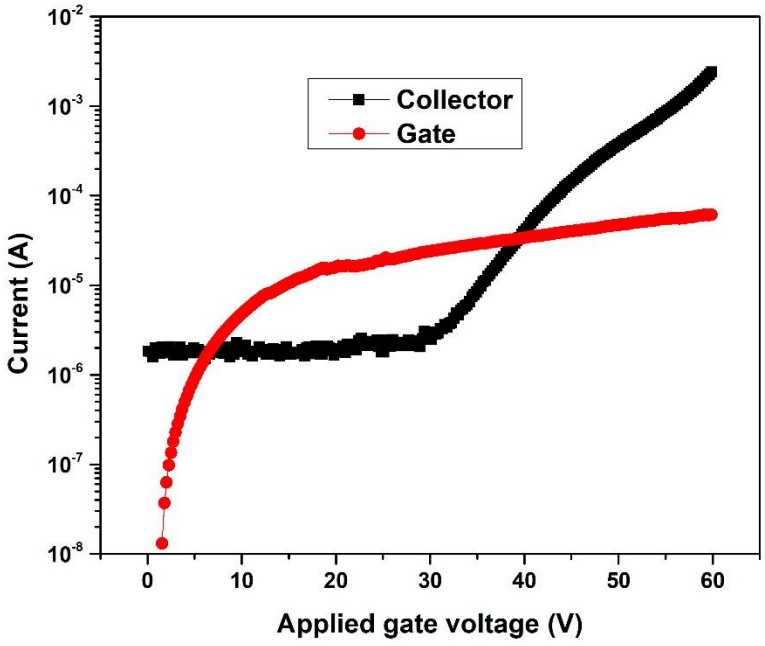


Figure III.2. Gate and collector, I-V characterization of a die.

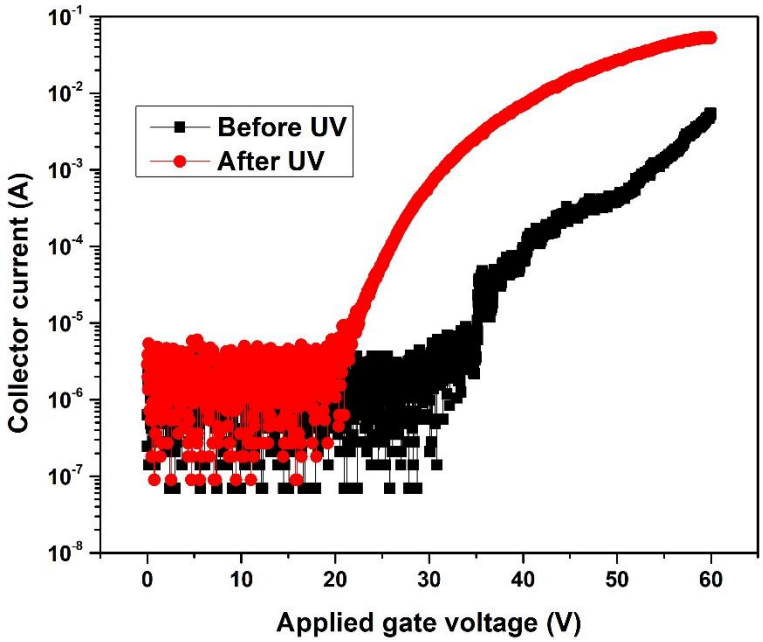


Figure III.3. I-V characterization comparison of collector current from a good die with respect to before and after UV exposure.

# Chapter IV. Experimental results of planar crossed-field device.

## Introduction

A simple, planar electrode system of 10 cm wide and 20 cm long with a gap of 2 cm has been used for the experiment. The experimental test structure is shown in Fig. III.1. Here a separate cathode is used in a beam injection mode to launch electrons into the crossed-field space between a sole electrode and an anode. This region of interest is used for our study. Mainly, two parameters were studied experimentally which were also be benchmarked using simulation and theory. A list of experimental parameters is given in Table IV.1.

*Table IV.1: Planar Crossed-Field Studies*

A. Experimental setup

| Parameters | Value | Type of Study |
|---|---|---|
| Magnetic field | 0.0 T to 0.02 T | Experiment |
| Effect of tilted magnetic field | $0^o$ to $5^o$ | Experiment |

A planar electrode system of 10 cm wide and 20 cm long with a gap of 2 cm has been used for the experiment. A test circuit was developed to drive the field emitters and collector the data which were sent to the PC using LabView. The schematic of the test circuit can be seen in fig. IV-1. The high voltage parts were isolated form ground using the in-house developed optical isolator boards. These boards were also used to send and receive the data to and from the high voltage side. The in-house developed test circuit installed in a high voltage isolation box can be seen in fig. IV-2. The sole electrode was kept at -3000V while the electron source emitter was kept at +200 V relative to the sole (-2800 V). Anode is fixed at ground. The anode-cathode distance was 20 mm. Here signal form the LabView program were sent to a microcontroller board through the optical isolator board. The microcontroller board then activates the driver pulse (+60 V relative to the emitter) for the GFEA's and the measured current were sent back to the PC using the same microcontroller board. The current at segmented anode and end collector were measured directly by LabView using resistors.

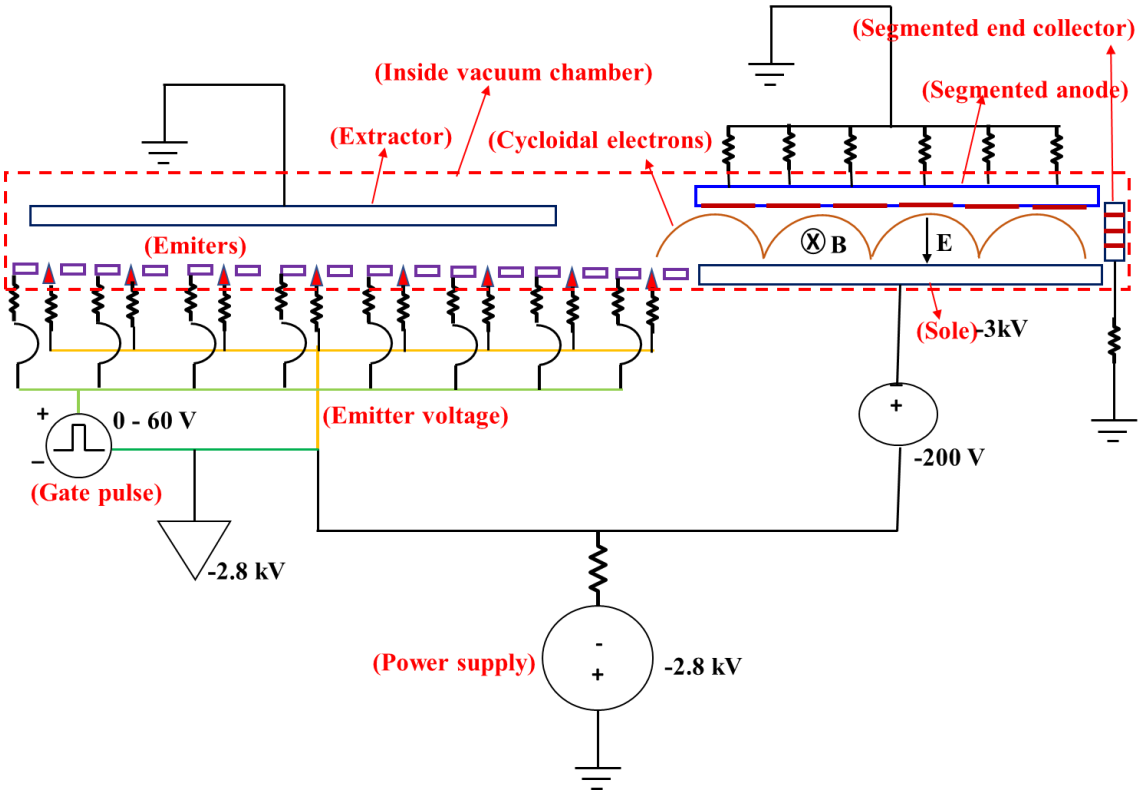


Figure IV.1. Schematic test circuit for the planar crossed-field experiment.

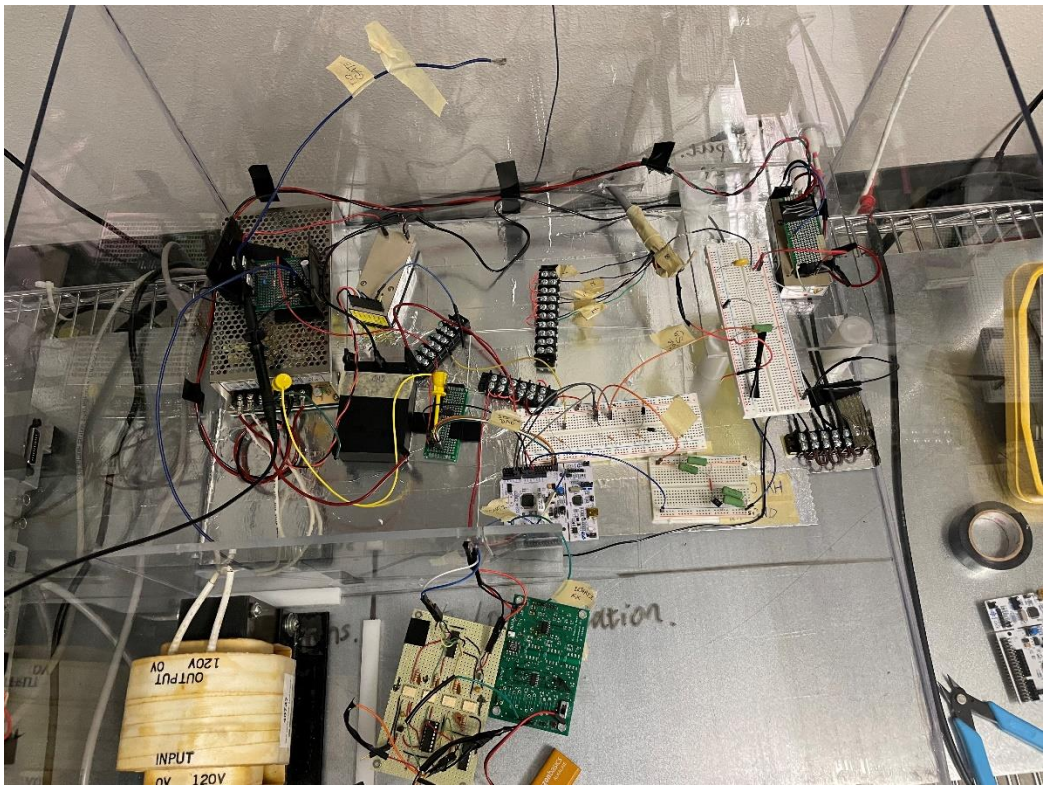


Figure IV.2. High voltage isolation box with the test circuit.

B. Experimental results

The magnetic field strength was varied from 0.01 T to 0.02 T with a step size of 0.01 T to look at the Hull cutoff. From Figure IV.4 it is clearly verifiable that electron beam behaving according to expectation. The first criterion is to have the magnetic field high enough to insulate the anode. Our goal is to operate with low enough current density to be stable when the magnetic field is above the Hull cutoff.

$$B_{HULL} = \sqrt{\frac{2mV}{eD^2}} \qquad \ldots\ldots\ldots (1)$$

For -3 kV sole voltage, $B_{HULL}$ is above 0.01 T for the 20 mm gap. For the below $B_{HULL}$ , a magnetic field of 0.009 T was applied and for the above $B_{HULL}$ case, a magnetic field of 0.012 T was applied. From the fig. IV.4, it was also clear that the for the bellow $B_{HULL}$, most of the electron hits the extractor where for the above case, most of the electron hits the end-collector.

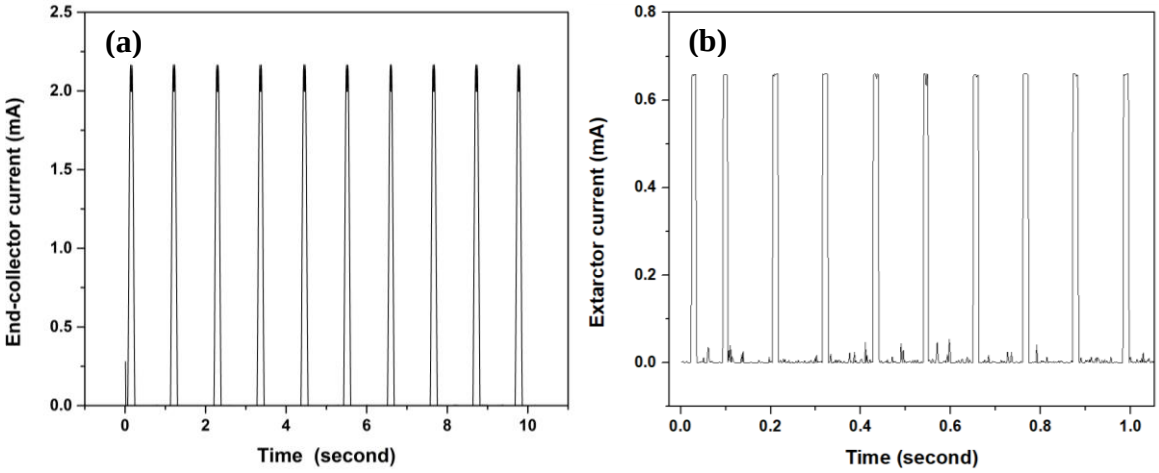


Figure IV.3. Extractor current (a) below $Hull_{cuoff}$ and (b) above $Hull_{cuoff}$

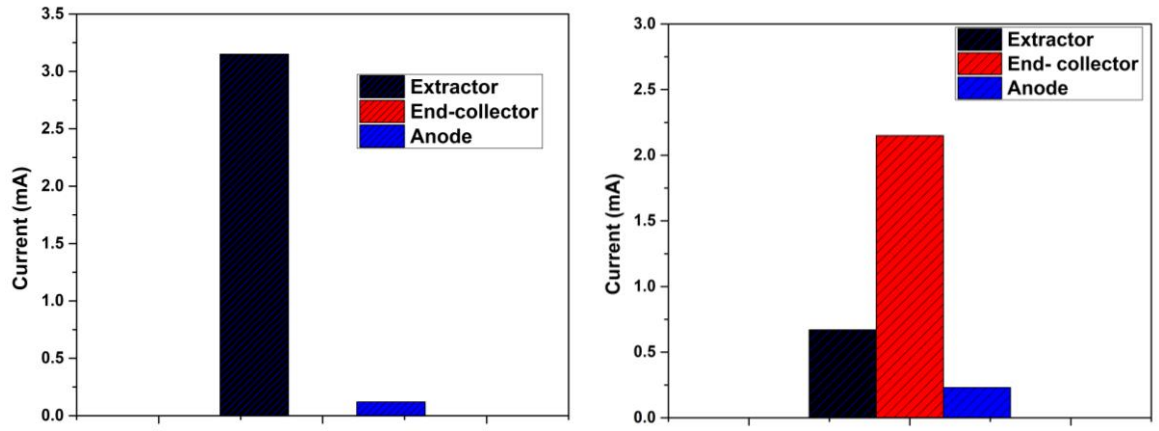


Figure IV.4. Comparison between different electrodes for the (a) below $Hull_{cuoff}$ and (b) above $Hull_{cuoff}$

Figure IV. 5 shows the effect of applied magnetic field of 0.2 T. Figure IV. 5(a) shows the simulation and Figure 5. (b) shows the experimental result. From the Figure 5, it can be deduced that the simulation and the experimental result matches well. The effect of a tilt in the magnetic field has also been studied for comparison with theory and experiment. The theory explains tilting the axis causes instability in beam propagation to occur at currents lower than the typical crossed-field critical current $J_c$ [47]. According to the theory and simulation results, tilting 1° produces complete breakdown at much below the typical $J_c$. Figure IV.6 shows a comparative beam position for a (a) no tilt and (b) a $5^o$ magnetic field tilt. From the fig. IV. 6, it can clearly be observed beam started tilting and the orbits traverse to the anode, which ultimately forms an unstable beam trajectory.

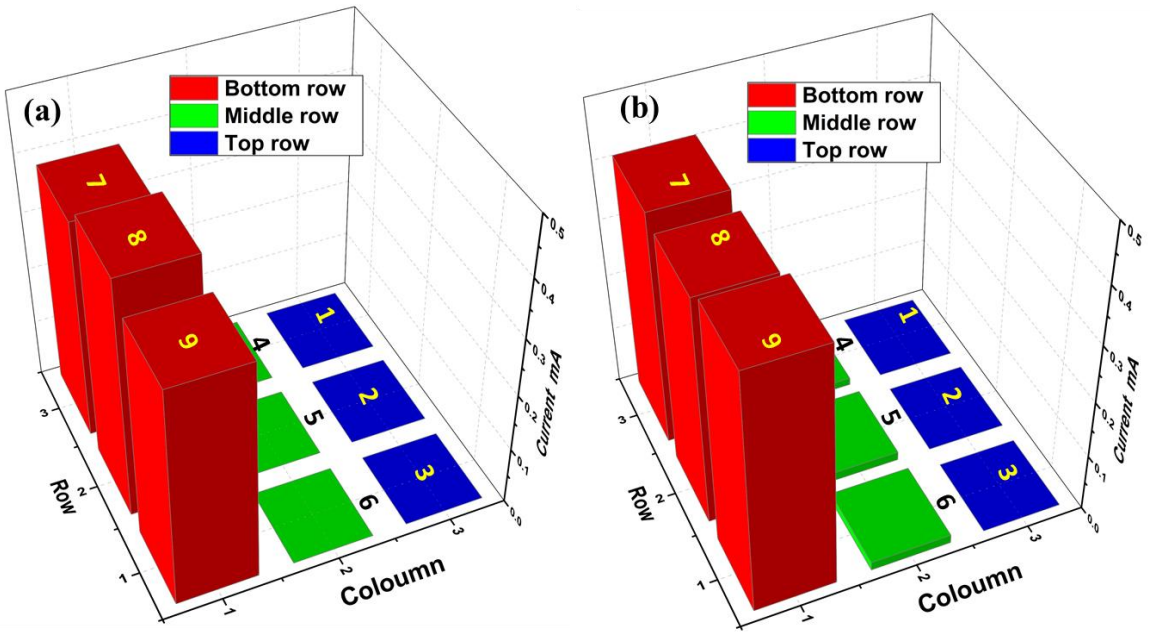


Figure IV.5. Effect of applied magnetic field of 0.02T (a) simulation and (b) experiment.

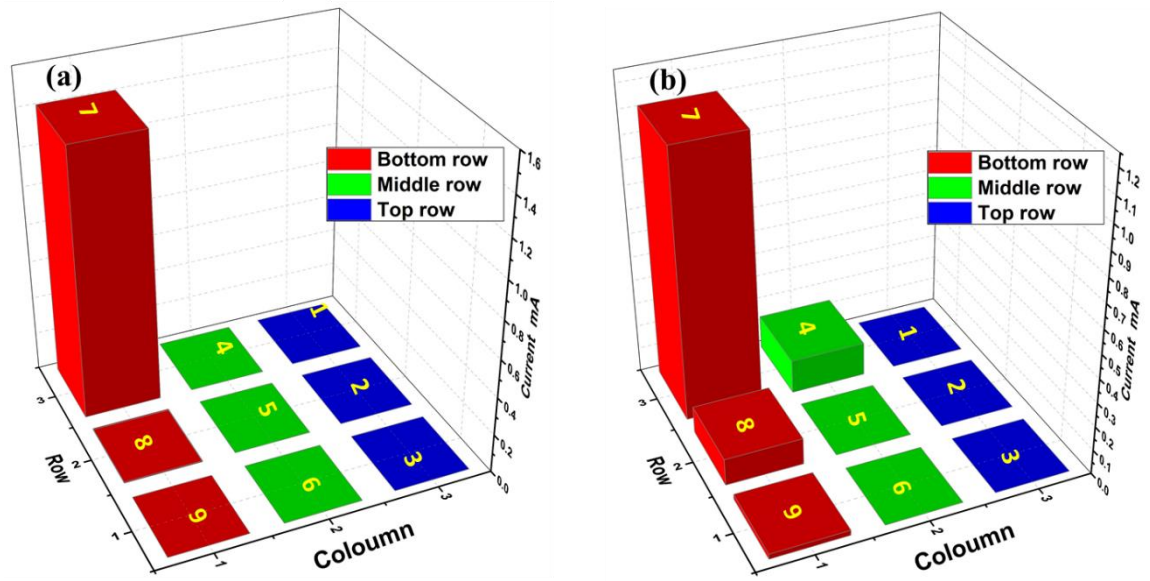


Figure IV.6. Effect of magnetic field tilt. Applied magnetic field is 0.02 T (a) simualtion and (b) experiment.

# Chapter V. Magnetron Simulation (BSU)

Electron Counter Injection Analysis

Definition

"Electron Counter-Injection" refers to the act of emitting electrons from the magnetron cathode with an initial azimuthal velocity with a direction that is *counter* to the direction of expected spoke rotation determined by the direction of the applied magnetic field.

Background

Previous studies have found there exists possible links between the level of cycloidialness of the electron population and magnetron start-up. It was observed that the azimuthal breadth ratio, which is the ratio between electrons moving in the direction of spoke rotation and electrons moving in the opposite direction of spoke rotation, consistently dip to lower levels and azimuthal velocities of the electrons seems to be significantly below the π-mode phase velocity (as shown in Figure V.1) prior to oscillation start, which indicates the electron population had heightened levels of cycoloidalness prior to start-up. The current study investigates the relationship between electron counter-injection and magnetron start-up. *Electron counter-injection is expected to increase the level of cycloidalness of the electron population.* All studies were conducted in PIC simulation using VSim.

The 2D Rising Sun magnetron (10-vane) model was used for this study. By default, this model oscillates under uniform electron emission with the emitted electrons having zero initial velocities in all directions and the electron spokes rotate in the clockwise direction. Counter-injection could alter the level of cycloidalness of the electron population in two ways. First, the level of cycloidalness can be altered by directly changing the amplitude of the initial azimuthal velocity; second, the level of cycloidalness can be altered by changing the percentage of the electrons that are counter-injected.

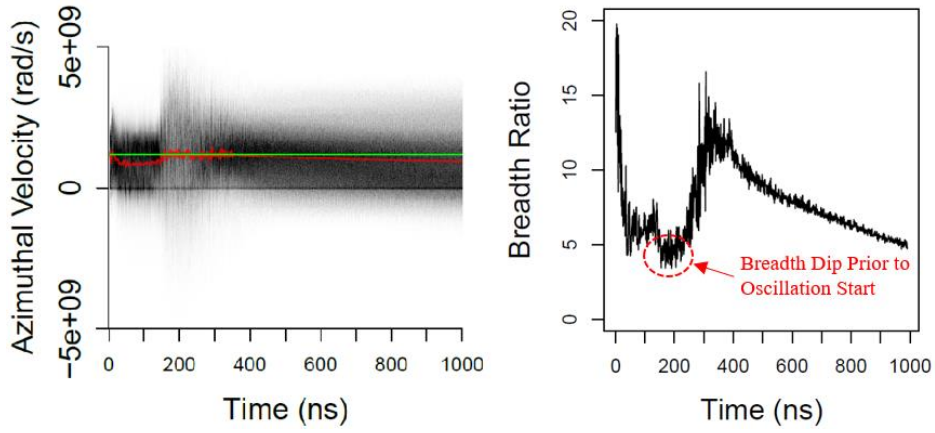


Figure V.1: Results from a 2D Rising Sun Magnetron Simulation. Left: Azimuthal velocity distribution with average (red line) and calculated π-mode phase velocity (green line). Right: azimuthal breadth ratio.

For the sake of simplicity, in this study, a fixed initial azimuthal velocity with an amplitude of 5.33e7 m/s in the counter-clockwise direction was applied. This velocity was determined by iterative parameter sweeps and 5.33e7 m/s seems to induce π-mode oscillation the best. Now, the level of cycloidalness can be altered by changing the percentage of electrons that are counter-injected.

Results

The ratio of counter-injection was swept from 0 to 1 in 0.1 increments, which results in 11 cases in total. When the ratio is 0, all electrons were injected uniformly, this is the reference case. On the other hand, when the ratio is 1, all electrons were counter-injected. By the same logic, a ratio of 0.6 indicates 60% of the electrons were counter-injected while the other 40% were injected uniformly. Each set of results to be shown below contains the electron distribution plots of 11 cases at various times.

Figure V.2 shows the electrons distributions at 25 ns, which is very early on in the simulation. Two things to be noted here. First, the electron counter-injection results in a much wider electron hub. This is expected because the counter-injection causes the cycloidal loop of the injected electron to be larger, as implied by the Lorentz force equation. Second, with increasing counter-injection ratio, spoke formation becomes more and more pronounced. The contrast between the 0.0 case (full uniform injection) and the 1.0 case (full counter-injection) is quite dramatic with the full uniform injection case showing a very narrow hub without any obvious spoke patterns and the full counter-injection case showing clear spoke patterns.

Figure V.3 shows the electrons distributions at 75 ns. This figure showcases the effects of the counter-injection with drastically different plot patterns under different counter-injection ratios. Clear five-spoke π-mode patterns can be seen in the 0.5 case and the 0.8 case; these two cases are at the onset of oscillation. Curiously, the 0.6 and 0.7 cases do not seem to produce clean π-mode patterns despite being in-between cases that worked well. The three cases from 0.0 to 0.2 seem to display three-spoke patterns with the cases with counter-injection having more spread-out spokes. The 0.3 and 0.4 cases show four-spoke patterns. The 0.9 and 1.0 cases failed to form any clean spoke patterns. Start-up behavior does not simply improve with a higher counter-injection ratio, instead, there seem to be certain “sweet spots” that work much better than the others.

Figure V.4 shows the electrons distributions at 150 ns. The 0.5 and 0.8 cases are now oscillating in the π-mode, but the five-spoke pattern is not “clean,” with the “halos” around the spokes, due to the counter-injection injecting electrons out-of-phase. The 0.0 reference case is at the onset of oscillation with its clear five-spoke pattern that is not yet fully formed. The 1.0 case is now a complete mess and once again suggests full counter-injection is not preferable.

Figure V.5 shows the electrons distributions at 300 ns. All cases other than the 0.9 and 1.0 cases are now oscillating in the π-mode. The reference case has the cleanest five-spoke pattern and the other cases with counter-injections all have “halos” around the spokes.

Discussions

These results seem to suggest a few things. First, electron counter injections have effects on the start-up process, though the physical mechanisms by which these effects take place are not yet clear at this point. Second, electron counter-injection, when applied correctly, clearly speeds up spoke formation and shortens oscillation start-up time. Third, after the magnetron is fully

oscillating, counter-injection seems to be of no further help to the characteristics of the oscillation, rather, it seems to produce noise. These results seem to suggest that the dominant physical process governing the magnetron's operation is different during start-up compared to when the device is in steady-state.

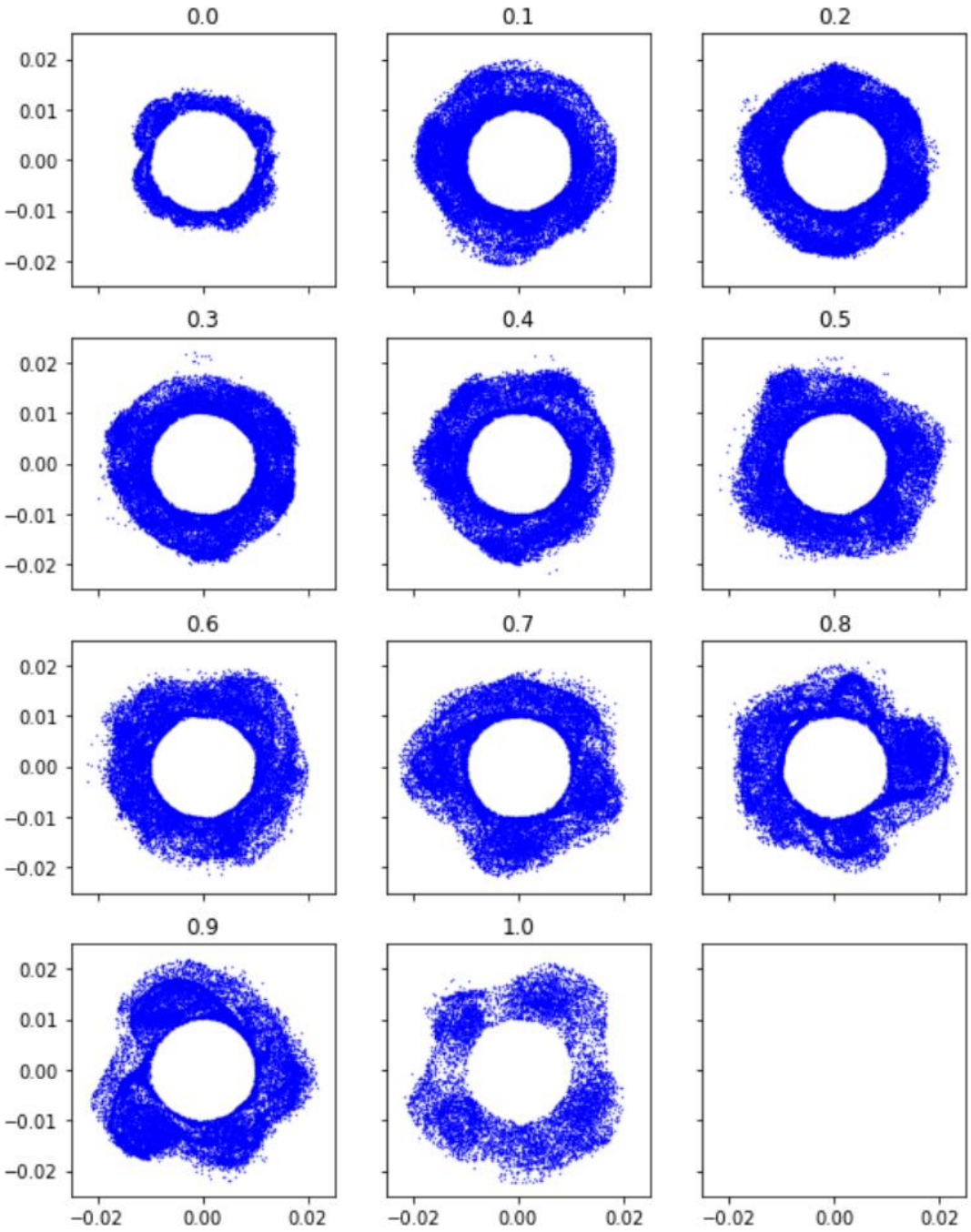


Figure V.1: Electron distributions at 25 ns under various counter-injection ratios (listed above each sub-figure).

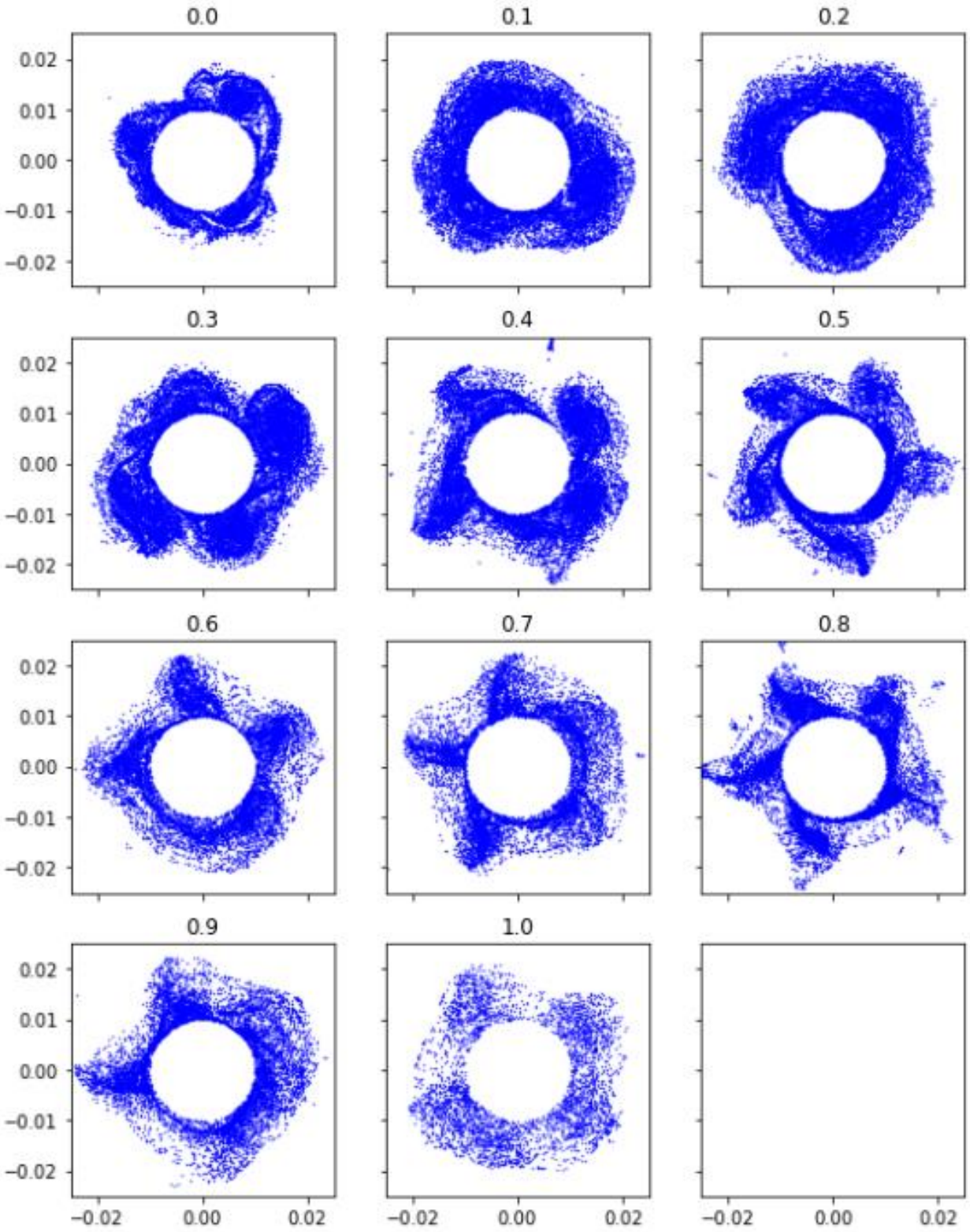


Figure V.3: Electron distributions at 75 ns under various counter-injection ratios (listed above each sub-figure).

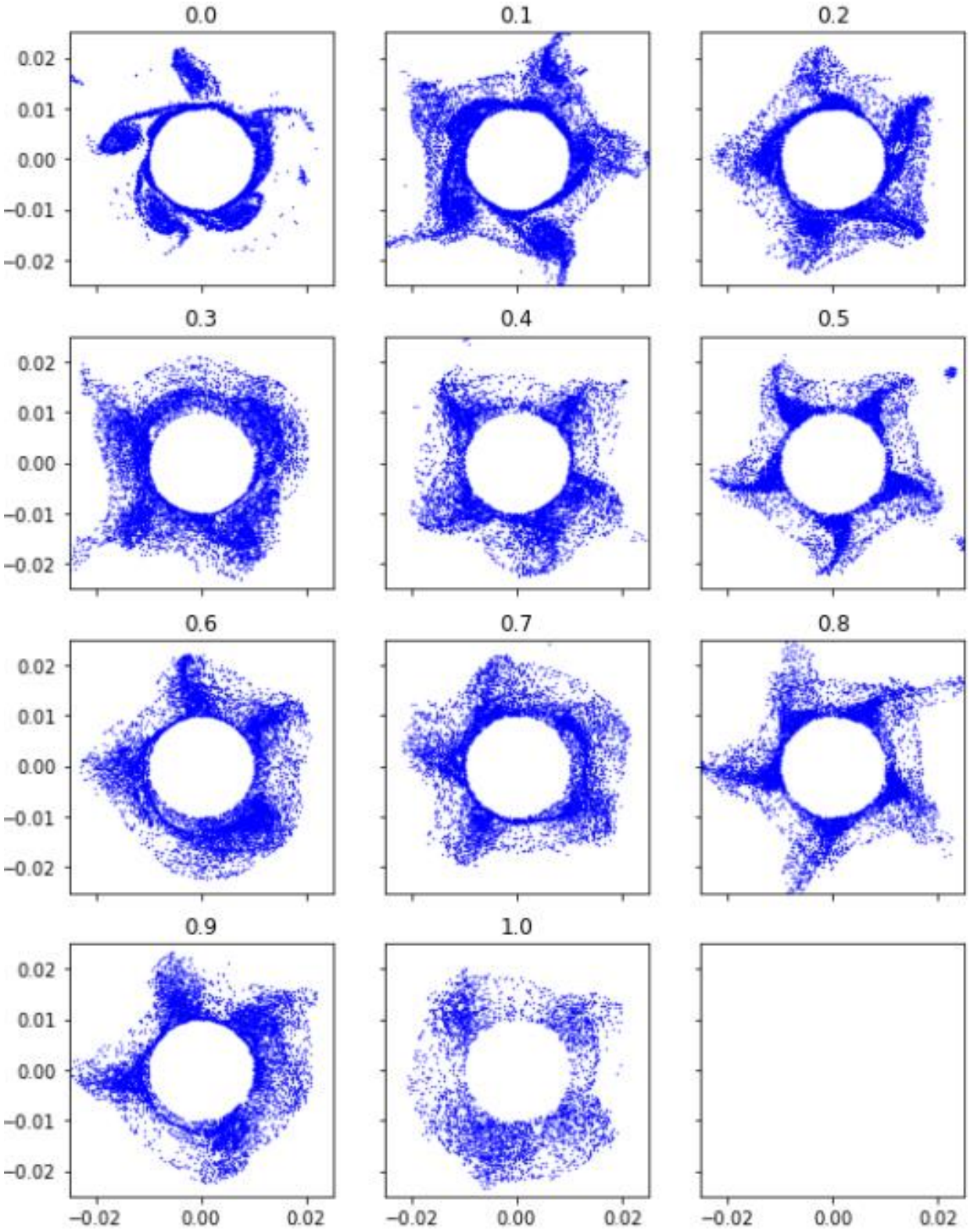


Figure V.4: Electron distributions at 150 ns under various counter-injection ratios (listed above each sub-figure).

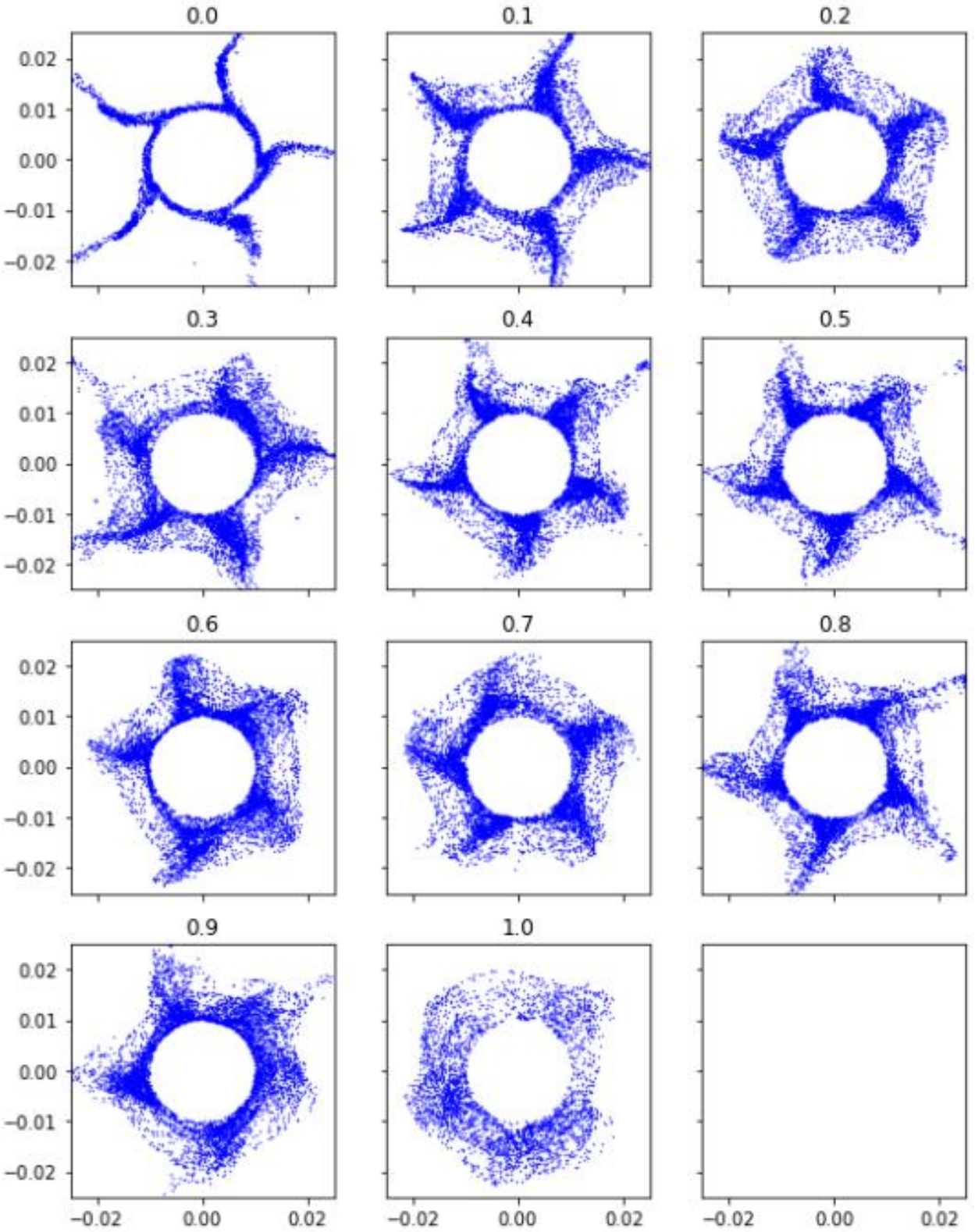


Figure V.5: Electron distributions at 300 ns under various counter-injection ratios (listed above each sub-figure).

Brillouin Flow Investigation.

Some preliminary work was done on studying the physics of the electron population via the simulation of a model with a simple coaxial geometry. The coaxial model studied in recent simulations is a 2D model with a cathode radius of 0.01 m and an anode radius of 0.0244 m. The cathode and anode radii are the same as that of the 2D Rising Sun magnetron model; the major difference between the coaxial model and the Rising Sun magnetron model is that the coaxial model does not contain any resonant cavities. The goal is to first study the physics of the electron population when it is not subjected to perturbation due to the resonant cavities; then the results can be compared to the 2D Rising Sun magnetron simulation results. This work is currently ongoing; the following section will discuss some preliminary results.

The coaxial model was first simulated with parameters and setups that are identical to the one used in the 2D Rising Sun magnetron simulation with no priming. Additionally, current injection was shut off at 40 ns. The reason for shutting down electron injection at 40 ns is to prevent the statistics of the electron population over time from being distorted by newly injected electrons. This simulation yielded the breadth ratios shown in V.6. The breadth ratio in radius stayed near 1:1, indicating that the electron population had no net movement toward the anode. This is expected since the geometry is coaxial, and the device is operating under the Hull cutoff. The breadth ratio in azimuth offered extremely interesting insights. As electron injection was shut off at 40 ns, after which point there was no new electron entering the interaction space, the breadth ratio in azimuth exploded to as high as 240:1 positive. This observation suggests that the portion of the electron population that had stayed in the interaction space for some time (i.e., electrons that are not newly injected) exhibited behaviors that are close to Brillouin flow. Additionally, the breadth ratio in azimuth after 40 ns showed an oscillation pattern, suggesting the presence of some instability that is periodic in nature. The precise indications of these observations are subjects for future work.

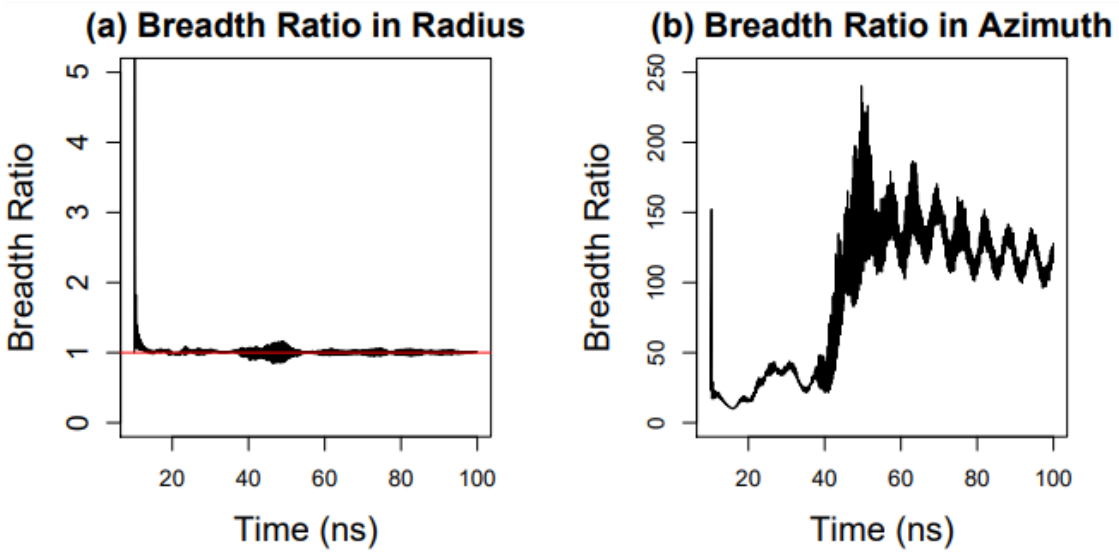


Figure V.6: Breadth ratios for the coaxial model with current injection being shut off at 40 ns.

Another analysis scheme currently in development aims to track the change of the electron trajectories' cycloidal radius over time. The current algorithm is only capable of tracking electrons one by one. The algorithm first organizes the electron's trajectory in temporally sequential order; then this sequence breaks down into temporal segments, each with the length of one RF period. Finally, the algorithm evaluates the difference between the smallest radial distance and the largest radial distance of the electron's trajectory within each RF period and plots the differences ("radial Δ") vs. time. V.7 shows the resulting

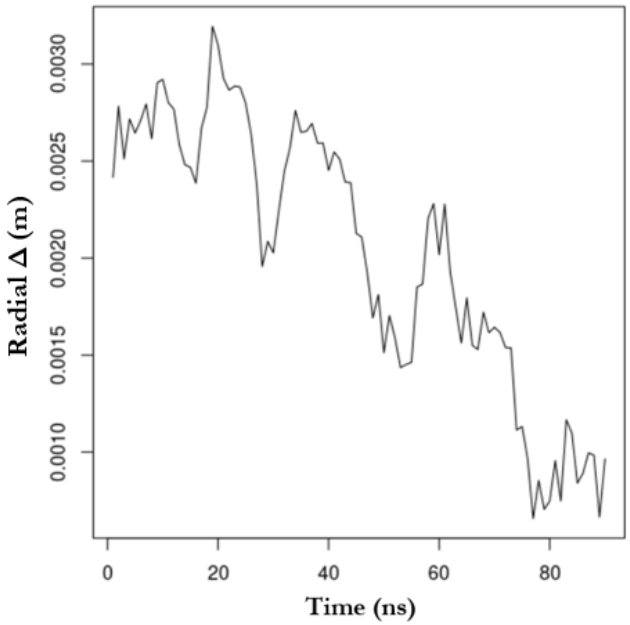


Figure V.7: Resulting plot from the radial Δ analysis for a single electron in the simulation of the coaxial model.

plot from the radial Δ analysis for a single electron in the simulation of the coaxial model. The plot shows the radial Δ decreased over time, which suggests the electron was becoming less cycloidal as time progressed. If an electron is in ideal Brillion flow, the radial Δ is expected to be near-zero. No meaningful conclusion can be reached based on V.7 since it is the analysis result of only a single electron; however, as the scale of the analysis expands, the goal is to perform this analysis to every macroparticle within the simulation and construct a statical distribution of radial Δ vs. time.

# Chapter VI. Development and Fabrication of Gated Field Emission Arrays for Experiment (MIT)

The GFEA die designed for both the Crossed-Field and Magnetron aspects of the experimental work have been under development and fabrication at MIT. A new fabrication process was developed this last year to improve emission uniformity of the GFEA die used in this project. Fabrication for Boise State University was repeated at MIT with one major change: a recently optimized (2019) photolithography process that enables improved reliability and performance over the previous round was substituted to conventional lithography without an antireflective coating. Minor optimizations were also completed along the way to improve the overall uniformity and expected die yield across the wafers. The major modification to the process utilizes an antireflection layer and a dielectric etchstop underneath the photoresist to minimize reflections to only a few percent, improving the edges of the original photoresist dot which results in a more circular dot required for high tip yield. Previous attempts demonstrated working FEAs with performance which was not sufficient for operation due to the single digit tip yield as calculated from electrical data.

The process was repeated to achieve a target neck width of ~100 nm before oxidation, but with a more optimized tip etch geometry and highly vertical nanowire in order to ensure that there is no bending of the nanowires occurs after the back-fill process. A comparison of the process, Figure V.1, shows the improvement in the fabrication after optimizations were ported onto the Boise State University mask layout. In the improved process flow, the aspect ratio of the neck is higher which is desirable due to the improved likelihood of a sharp tip after oxidation. The nanowire etch is now more vertical providing for more space between the nanowires for the dielectric fill process. The nanowire to nanowire uniformity has also improved due to improvements to all of the above.

After the nanowire are fabricated, the same fill pattern is repeated where the nanowire is oxidized, polysilicon is deposited and subsequently oxidized. Finally low-stress Si-rich nitride is deposited as the final fill layer. After this process, the wafers show the uniform dot pattern that is expected of a well-fabricated FEA, Figure V.2, and the wafer shows good across-wafer uniformity at this stage. Following the dielectric fill, CMP was performed with an improved slurry selection which has benefited the across-wafer uniformity relative to the previous round. The target gate depth was again 200 nm, though some portions of the wafer have larger depths. The polysilicon gate was deposited and CMP was performed on the wafers to reveal the oxide dome before nanowire release. The SEM images, Figure V.3, illustrate the improved overall quality of the wafers. While both final aperture sizes are 200 nm in diameter, the improved lithography and dry etch yields an orderly array of dots.

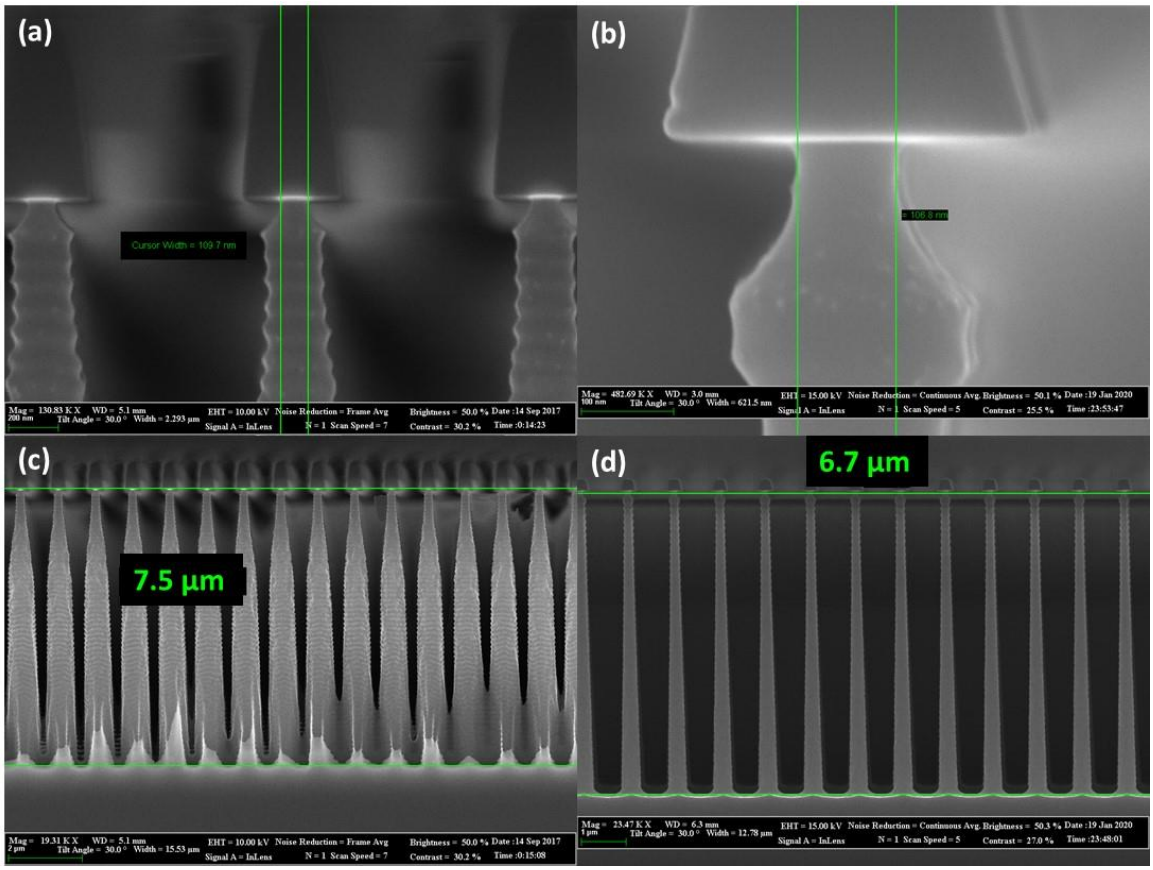


**Figure VI.1**. Cross section of the process in (a,c) 2017-2018 vs. 2019-2020 (b,d). The zoomed SEMs of the tip show illustrates that while the neck size still targets ~100 nm, the aspect ratio is different (higher). Furthermore, the verticality of the dry etch has been improved resulting in a significant gap between the nanowires to prevent bending of the nanowires later in the process. Finally, the nanowire to nanowire variation has been reduced, this can be observed by the spacing between nanowires becoming more uniform.

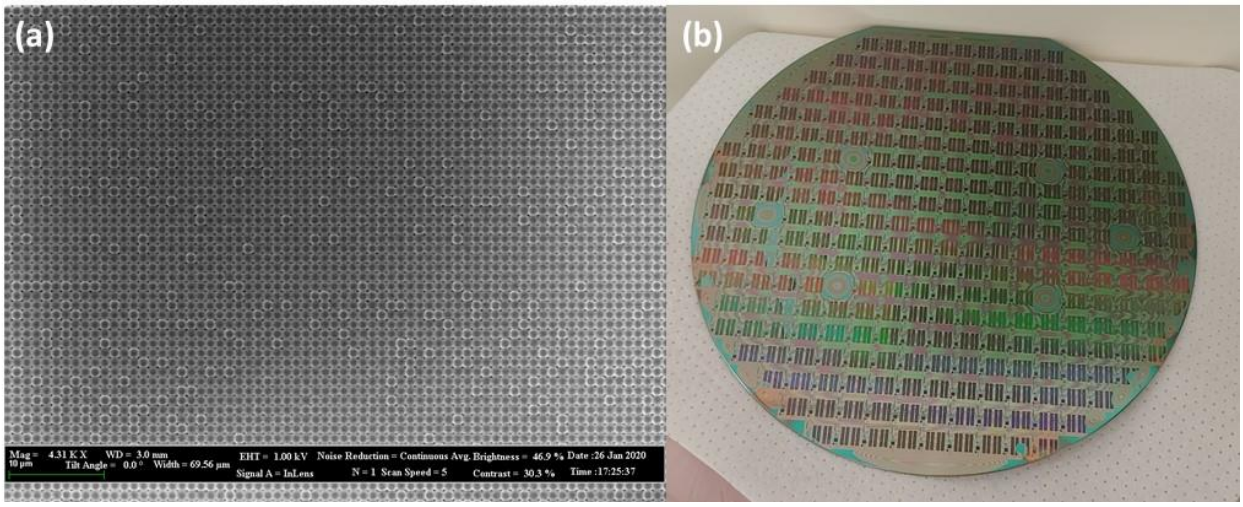


**Figure VI.2**. (a) SEM of wafer after the dielectric fill process. The domes show a uniform unit cell which indicates that the spacing of the nanowires are uniform. (b) Photo of wafer after nitride deposition showing uniform color across the horizontals due to the diffraction of light.

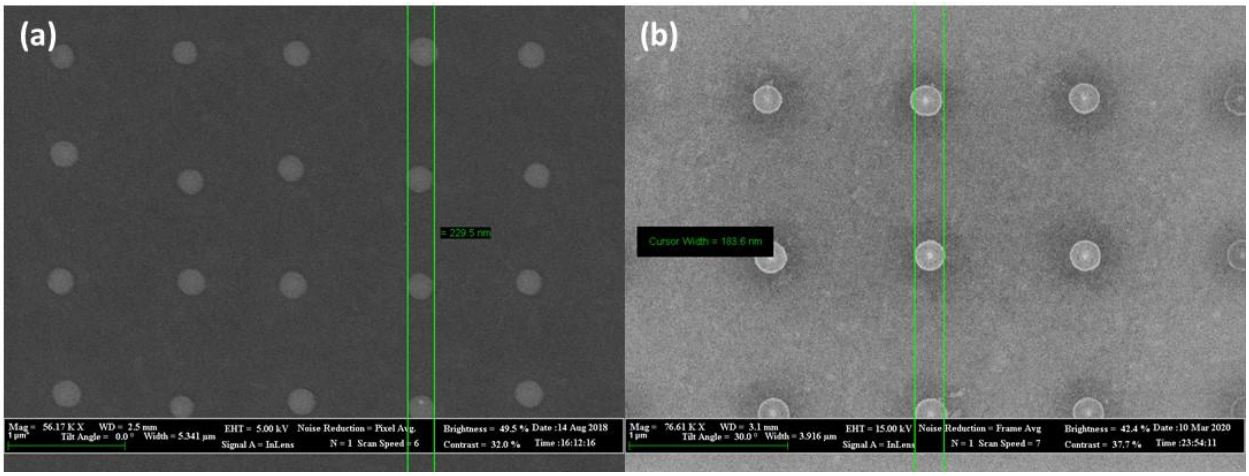


**Figure VI.3**. Devices after polysilicon CMP with the gate cap revealed in the (a) previous and (b) current fabrication run. The order of the nanowire pitch is excellent with the current process improvements.

# Chapter VII. Theoretical Crossed-Field Development (Purdue)

The goal of this portion of the grant was to develop a first-principles based theory for the maximum current permissible in a one-dimensional (1-D), nonplanar crossed-field diode. This required us to first revisit the concept for the maximum current permissible in a 1-D nonplanar diode without a magnetic field. We used the technique of variational calculus, which extremizes a quantity, namely the current in the gap, to derive a coordinate-system invariant solution of the space-charge limited current (SCLC) that can be applied to any geometry for which one could determine the Laplacian and gradient of the electric potential. We then derived equations for SCLC for 1-D concentric spheres and concentric cylinders.

In the process, we determined that the solution obtained by Langmuir and Blodgett for cylinders and spheres nearly a century ago was not the "true 1-D" SCLC. Furthermore, we learned that one cannot directly apply the concept of continuity from Maxwell's equation since that is only valid in three-dimensions (3-D). Reducing the physical geometry from 3-D to 1-D necessitates accounting for the elimination of the other two coordinate systems. In Cartesian coordinates (i.e., Child-Langmuir for SCLC for a 1-D planar diode), the standard continuity relationship can be used; however, for other coordinate systems, such as spherical and cylindrical, a correction is necessary when applying continuity in 1-D because the unit vectors are not independent. Because the coordinates are linked when doing the mathematical analysis, one must introduce a correction factor in spherical and cylindrical coordinates to appropriately account for the translation to 1-D.

We next obtained solutions for 1-D SCLC of a cylindrical diode in a crossed-field device both below the Hull cutoff magnetic field (the maximum magnetic field for an which an electron emitted from the cathode just reaches the anode with zero velocity in the direction across the gap) and above the Hull cutoff. Future work is exploring extensions to other geometries. We also assessed the implications of a series resistor on magnetic insulation and stability for 1-D planar devices near, but just below, the Hull cutoff.

We summarize the key results for these problems in the following sections.

## Derivation of Space-Charge Limited Current in 1-D Nonplanar Diodes Using Variational Calculus

**[FEATURED ARTICLE]** A. M. Darr[G] and **A. L. Garner**, "A Coordinate System Invariant Formulation for Space-Charge Limited Current in Vacuum," *Applied Physics Letters* **115**, 054101 (2019). **[Selected for Featured Article:** https://doi.org/10.1063/1.5121645]

The first year of this effort focused on deriving space-charge limited emission using variational calculus in preparation for applying it to a crossed field geometry in Year 2. This work was published in *Applied Physics Letters* [A. M. Darr and A. L. Garner, "A Coordinate System Invariant Formulation for Space-Charge Limited Current in Vacuum," *Applied Physics Letters* **115**, 054101 (2019).]. This paper was selected as a featured article [https://doi.org/10.1063/1.5121645].

The space-charge limited current (SCLC) in vacuum was first derived by Child [1] for planar geometry and by Langmuir for planar and coaxial cylindrical geometries [2]. Initially attributed to residual gas effects [2], the poor agreement between experiments and theory for cylindrical SCLC was later attributed to secondary emission [3]. Simulations also significantly disagree with theory for cylindrical SCLC [4]. The Child-Langmuir (CL) law calculates planar SCLC; the Langmuir-Blodgett (LB) equations model SCLC for cylinders and spheres [1,2,5,6]. Classical CL and LB were derived for one-dimensional (1D) geometry assuming zero injection velocity. Subsequent theories have extended these calculations to non-zero injection velocity [7-10], multiple dimensions [11-15], and multiple charged species [16].

Characterizing geometric effects on SCLC is important for designing modern devices, particularly magnetrons and nanodevices [17-21]. Many studies have added precision to LB [7,8,22], applied numerical methods [23-28], derived transit time models [29,30], or made analytic approximations assuming no space-charge [31,32]. In this Letter, we derive an analytical solution of Poisson's equation using variational calculus (VC) to calculate SCLC. Although numerical VC techniques have been used for SCLC [27,28], we derive exact, closed-form solutions for SCLC in 1-D planar, cylindrical, and spherical coordinate systems by starting from a coordinate system invariant representation obtained from first principles.

Combining continuity, conservation of energy, and Poisson's equation gives the SCLC as

$$J = \epsilon_0 \nabla^2 \phi \sqrt{2e\phi/m}\,, \tag{1}$$

where $J$ is the current density, $\epsilon_0$ is the permittivity of free space, $\phi$ is the electric potential, $e$ is the electron charge, and $m$ is the electron mass. While our initial work considered extremizing power as a way to justify extremizing the average current in the gap [29], it is mathematically equivalent to instead average the current directly [30]. In fact, if one considers SCLC as representing the maximum current possible to inject into the gap, this latter definition is more in keeping with the physical definition, although this comes out to be more of a philosophical debate than a practical difference [30].

VC SCLC for the potential in a general coordinate system $s$ $\phi(s)$ by solving the Euler-Lagrange (EL) equation of the current using the appropriate diode boundary conditions. In general, the EL equation for $N$ general coordinates $k$ is [31]

$$\frac{\partial f}{\partial \phi} + \sum_{k=1}^{N} \frac{\partial^2}{\partial k^2}\left(\frac{\partial f}{\partial \phi_{kk}}\right) - \frac{\partial}{\partial k}\left(\frac{\partial f}{\partial \phi_k}\right) = 0 \tag{2}$$

with partial derivatives denoted by subscripts ($\phi_k \equiv \partial\phi/\partial k$) and $f$ is a function of $\phi, k$, and the partial derivatives of $\phi$. For a general coordinate system, we obtain

$$\nabla^2\phi = \frac{|\nabla\phi|^2}{4\phi}. \tag{3}$$

For boundary conditions, we set $\phi = 0$ at the cathode and $\phi = V_g$ at the anode with the area $A(s)$ depending on the coordinate system. For Cartesian coordinates, $A(x)$ is constant and we obtain

$$\phi_p(x) = V_g(x/D)^{4/3}. \tag{4}$$

Combining (3) and (4) gives the SCLC for Cartesian coordinates as

$$J_p = \frac{4V_g^{3/2}\epsilon_0\sqrt{2e/m}}{9D^2}, \tag{5}$$

which is the familiar CL law [1,2]. For cylindrical coordinates with axial and angular symmetry, $(R_c) = 0$ and $\phi(R_a) = V_g$ where $R_c$ and $R_a$ are the cathode and anode radii, respectively, and $A(r) \propto r$. This gives

$$\phi_c(r) = V_g\left[\frac{\ln(r/R_c)}{\ln(R_c/R_a)}\right]^{4/3}. \tag{6}$$

Combining (3) and (6) at $r = R_c$ yields

$$J_c = \frac{4V_g^{3/2}\epsilon_0\sqrt{2e/m}}{9R_c^2(\ln\bar{a})^2}, \tag{7}$$

for the VC cylindrical SCLE with $\bar{a} \equiv R_c/R_a$. Equation (7) is an exact, closed-form solution from first principles that makes no assumptions on the form of $\phi_c(r)$. In comparison, LB used a series solution of (3) assuming $I \propto 1/(r\beta^2)$, yielding

$$J_{c,LB} = \frac{4V_g^{3/2}\epsilon_0\sqrt{2e/m}}{9R_cR_a\beta^2}, \tag{8}$$

with cylindrical geometric effects captured by $\beta = \beta(\bar{a})$, initially calculated for discrete increments of $\bar{a}$ using a power series expansion centered on $\bar{a} = 1$ [2,5,8,22].

Fig. 1(a) compares (7), (8), a theoretical approximation assuming $\phi'(r) = 0$ near the cathode [32], and a transit time model using the non-SCLE potential function [33] for a constant inner radius of 1 cm and $V_g = 1$ V. All theories converge as $\bar{a} \to 1$, which corresponds to small gap distance $D \equiv |R_a - R_c|$. In the small gap limit, $\ln(\bar{a}) \approx D/R_a$or $\ln(\bar{a}) \approx D/R_c$ for $R_c > R_a$ and $R_a < R_c$, respectively; for both cases, (7) reduces to (5). Physically, CL is the limiting behavior near $\bar{a} = 1$ because the anode and cathode surfaces are nearly parallel. The theories begin to disagree as $\bar{a}$ diverges from unity. As $\bar{a} \to \infty$, all theories agree within an order of magnitude and have similar

slopes; however, the theories diverge dramatically (over a few orders of magnitude), although still with similar slopes, as $\bar{a} \to 0$. Since Refs. [32] and [33] rely on assumptions violating SCLC, their close agreement with LB suggests that the traditional LB equations do not account for all relevant physics, especially for $\bar{a}$ far from unity, whereas the VC solution is based upon SCLC physics and analytic for all $\bar{a}$.

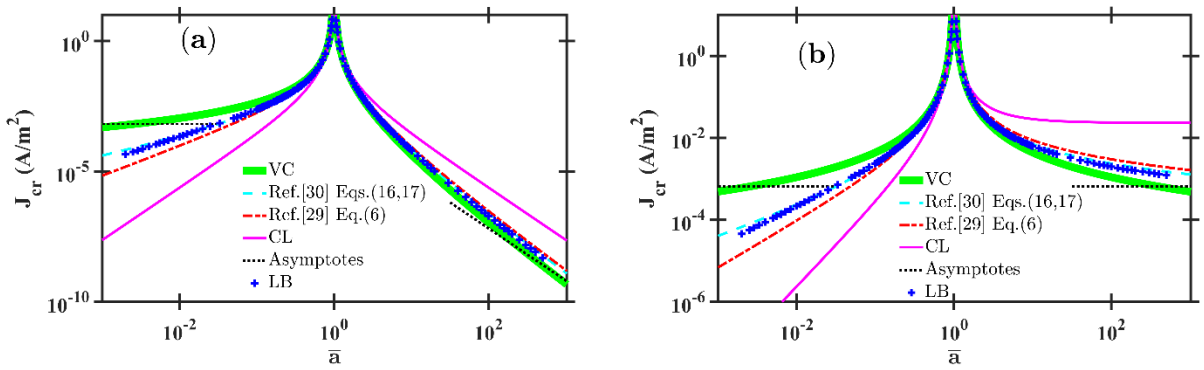


FIG. VII.1 – Space-charge limited emission current density $J_{cr}$ for coaxial cylindrical diodes in vacuum as a function of $\bar{a} = R_c/R_a$ with bias voltage 1 V, cathode radius $R_c$, and anode radius $R_a$ for (a) constant inner radius of 1 cm and for (b) constant $R_c = 1\ cm$. The thicker solid line is the variational calculus (VC) solution (7), the dashed cyan line assumes the electric field is zero near the cathode Ref. [32] (Ref. [30] in the figure) equations (16,17), the dot-dashed red line assumes a potential function with no space-charge and solves numerically using the transit time solution from Ref. [33] (Ref. [29] in the figure), the solid magenta line is the Child-Langmuir (CL) solution $J_p$ for planar geometry (5) with $D \equiv |R_c - R_a|$, the dotted black lines are the asymptotic limits of the VC solution (9) as $\bar{a} \to 0$ and $\bar{a} \to \infty$ for $ln(\bar{a}) \approx 6$, and the blue plus marks are the Langmuir-Blodgett (LB) solution (8) using a power series approximation of Poisson's equation centered around $\bar{a} = 1$.

To demonstrate the accuracy of the VC solution, we compared (11) and (12) with simulation data from a particle-in-cell simulation for a cylindrical geometry with $R_c = 0.005$ m and $R_a = 0.01$ m ($\bar{a} = 0.5$) [4]. LB gives $\beta^2 = 0.2793$ for $\bar{a} = 0.5$ [6]. Figure 2 shows that, even at $\bar{a}$ close to unity, VC agrees better with the simulation results than LB, while also giving closed form solutions. The benefit of VC as $\bar{a} \to 0$ or $\bar{a} \to \infty$ is most likely much more pronounced.

The slow variation of $\ln(\bar{a})^2$ as $\bar{a} \to 0$ and $\bar{a} \to \infty$ reduces (11) to

$$J_c|_{\bar{a}\to 0} = J_c|_{\bar{a}\to\infty} \approx \frac{4V_g^{3/2}\epsilon_0\sqrt{2e/m}}{9R_c^2\gamma^2} \propto \frac{1}{R_c^2}, \qquad (9)$$

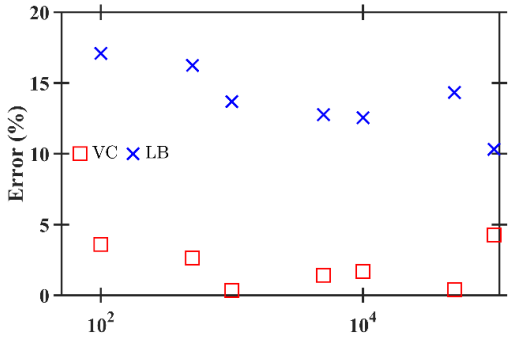


FIG. VII.2 – Relative difference between a particle-in-simulation [4] of space-charge limited emission current density $J_{cr}$ for a coaxial cylindrical diode with cathode radius 0.005 cm and anode radius 0.01 cm ($\bar{a} = 0.5$) as a function of bias voltage $V_g$ with either the variational calculus (VC) solution (7) or Langmuir-Blodgett (8).

for *both* limits, with $\gamma \approx \ln(\bar{a}) \approx \text{constant}$. Figure 1(b) plots the same theories as Fig. 1(a) with $V_g = 1$ V, but with constant $R_c = 1$ cm. The asymptotes in Fig. 1(b) are for $\ln(\bar{a}) \approx \ln(400) \approx 6 = \gamma$; this highlights the symmetry between external and internal cathode diodes. As $\bar{a}$ diverges further from unity (in either direction), (13) shows that $J_c$ and $I$ become nearly constant.

Noting $A(r) \propto r^2$ and assuming angular symmetry, we solve (7) for spherical geometry with boundary conditions $\phi(0) = 0$ and $\phi(R_a) = V_g$ [s] to obtain the spherical potential function

$$\phi_s(r) = V_g \left[ \left( \frac{R_a}{R_a - R_c} \right) \left( 1 - \frac{R_c}{r} \right) \right]^{4/3}. \tag{10}$$

Combining (10) with (3) at $r = R_c$ gives the VC spherical SCLE emission current density as

$$J_s = \frac{4 V_g^{3/2} \epsilon_0 \sqrt{2e/m}}{9 \bar{a}^2 D^2}, \tag{11}$$

where $D \equiv |R_a - R_c|$ is the gap distance. Analogous to the cylindrical case, (11) is an exact, closed-form solution from first principles that makes no assumptions on the form of $\phi_s(r)$. The original LB solution for spheres also used a series solution of (4), assuming $I \propto 1/(\alpha^2)$; this yields

$$J_{s,LB} = \frac{4 V_g^{3/2} \epsilon_0 \sqrt{2e/m}}{9 R_c^2 \alpha^2}, \tag{12}$$

with spherical geometric effects captured by $\alpha(\bar{a})$. A direct comparison between (15) and (16) suggests $\alpha^2 = (1 - \bar{a})^2$. Historically, $\alpha$ was calculated for discrete increments of $\bar{a}$ [6] or approximated as an equation [33]; other refinements assume a non-SCLE potential function across the gap and use the cathode electric field or solve for $J$ numerically using a transit time model [29]. The problems posed by these simplifications are unchanged from their appearance in the cylindrical case.

Figure 3(a) compares (11), (12), and Ref. [33] for a constant inner radius of 1 cm and $V_g = 1$ V; it shows that VC and the other theories agree well near $\bar{a} = 1$ where the solutions reduce to (5); the solutions converge to the CL law because the anode and cathode become nearly parallel as $\bar{a} \to 1$. As $\bar{a} \to 0$, the theories diverge significantly in slope and magnitude; however, as $\bar{a} \to \infty$, the non-SCLC field and potential solutions match closely with LB, while VC, which has a fully SCLC potential function, diverges by over an order of magnitude.

Asymptotically, the limits of (11) as $\bar{a} \to 0$ and $\bar{a} \to \infty$ are

$$J_s|_{\bar{a} \to 0} \approx \frac{4 V_g^{3/2} \epsilon_0 \sqrt{2e/m}}{9 R_c^2} \propto \frac{1}{R_c^2}. \tag{13}$$

and

$$J_s|_{\bar{a}\to\infty} \approx \frac{4V_g^{3/2}\epsilon_0\sqrt{2e/m}}{9\bar{a}^2R_c^2} \propto \frac{1}{\bar{a}^2R_c^2} = \frac{R_a^2}{R_c^4}, \tag{14}$$

respectively.

Figure 3(b) highlights (13) and (14) by comparing SCLC $J$ with $R_c = 1$ cm for all $\bar{a}$. As $\bar{a} \to 0$ $J$ is completely independent of $R_a$, whereas as $\bar{a} \to \infty$ there is an additional dependence upon $\bar{a}$. Physically, $\bar{a} \to 0$ represents a central emitting cathode with a distant, relatively large anode and $\bar{a} \to \infty$ represents a large outer emitting cathode with a relatively small anode. To understand the differences between these limits, we compare the total emission current. Multiplying $J$ by the cathode area shows that $I \propto$ constant as $\bar{a} \to 0$ and $I \propto 1/\bar{a}^2$ as $\bar{a} \to \infty$. While the original LB derivation noted that the total current emission was independent of sphere size and depended only upon $\bar{a}$ [6], our results further demonstrate that the current is also *completely* independent of $\bar{a}$ when $\bar{a} \to 0$; Fig. 3 shows that (15) approaches (17) rapidly. We hypothesize that the cathode appears as a point emitter to the anode at these small aspect ratios; therefore, increasing $R_a$ or decreasing $R_c$ no longer affects the total $I$. For $\bar{a} \to \infty$, the anode is now a point receiver, but we calculate *emission* current, so $\bar{a}$ is still important. We hypothesize that when $\bar{a}$ increases, the relative surface areas of the cathode and anode increase as $\bar{a}^2$ and the emitted electrons crowd together as they travel to the anode. The increased electric field reduces the space-charge limit. This does not occur as $\bar{a} \to 0$ because the emitted electrons spread out during their transit from the cathode to anode.

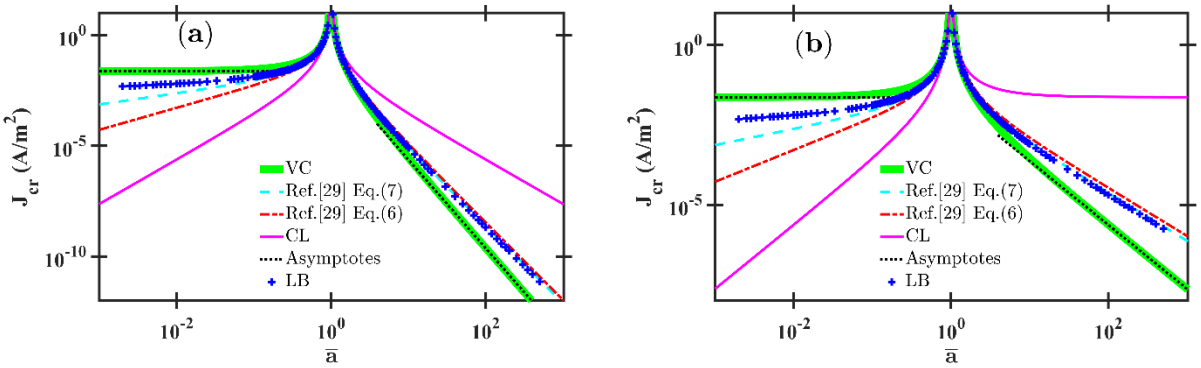


FIG. VII.3 – Space-charge limited current density $J_{cr}$ for concentric spherical diodes in vacuum as a function of aspect ratio $\bar{a} = R_c/R_a$ with bias voltage 1 V, cathode radius $R_c$, and anode radius $R_a$ for (a) constant inner radius of 1 cm and for (b) constant $R_c = 1\ cm$. The thicker solid green line is the variational calculus (VC) solution (15), the dashed cyan line assumes the cathode electric field is non-SCLC equation from Ref. [29], the dot-dash red line assumes a potential function with no space-charge and solves numerically using the transit time Ref. [29] equation (6), the solid magenta line is the Child-Langmuir (CL) solution $J_p$ for planar geometry (9) with $D \equiv |R_c - R_a|$, the dotted black lines are the asymptotic limits of the VC solution (17) as $\bar{a} \to 0$ and (18) as $\bar{a} \to \infty$, and the blue pluses are the Langmuir-Blodgett solution (12) which used a power series approximation of Poisson's equation centered around $\bar{a} = 1$.

A. M. Darr[G], N. R. Sree Harsha[G], and **A. L. Garner**, "Response to "Comment on 'A coordinate system invariant formulation for space-charge limited current in vacuum'" [Appl. Phys. Lett. 118, 266101 (2021)]," *Applied Physics Letters* **118**, 266102 (2021).

We next assess continuity. The results for concentric cylinders and spheres seem to violate steady-state continuity, as defined by [34]

$$\nabla \cdot \vec{J} = -\partial\rho/\partial t = 0, \tag{15}$$

with current density $\vec{J}$, charge density $\rho$, and time $t$. We reconciled the VC solutions with continuity [30] by examining the assumptions inherent in (15). Fundamentally, steady-state continuity demands that the amount of charge $q$ in a source-free region remains constant with time:

$$dq/dt + \oiint_S \vec{J} \cdot d\vec{S} = 0, \tag{16}$$

with differential area vector $\vec{S}$ for the closed surface $S$. Equation (16) commonly reduces to (15) using divergence theory; however, this assumes constant differential volume. This constraint always holds in *3-D* space; however, the VC derivation uses symmetric assumptions and only considers *1-D* space. When translating from 3-D to 1-D, the variation of differential volume for must accurately account for the coordinates orthogonal to $\vec{J}$. Translating from 3-D to 1-D in cylindrical and spherical coordinates is complicated since the coordinates are *not* independent – the angular components depend on the radial coordinate $r$, which must be explicitly considered.

For 1-D flow in the $x_1$-direction ($x_n$ are general coordinates), the differential form of (16) in steady-state is

$$\nabla \cdot (\bar{\chi}(\vec{x})\rho\vec{v}) = \nabla \cdot \left(\bar{\chi}(\vec{x})\vec{J}\right) = 0, \tag{17}$$

where $\bar{\chi}(\vec{x}) = \Delta x_2(\vec{x})\Delta x_3(\vec{x})$, $x_2$ and $x_3$ are orthogonal to the flow, and all coordinates may, in general, depend on the others [35]. Equation (17) holds for all orthogonal coordinate systems and – unlike (15) – is general for 1-D, 2-D, and 3-D. For 1-D planar, cylindrical, and spherical geometries, $\bar{\chi} = 1$, $r$, and $r^2$, respectively. Applying (17) to the cylindrical and spherical SCLC VC solutions [29] shows that they satisfy continuity. The confusion arose since $\bar{\chi} = 1$ only for Cartesian coordinates, so (17) reduces to (15) for planar alone. Charge is conserved and emission current is calculated self-consistently; the scaling proposed in [29] ($J_c \propto r^{-1}, J_s \propto r^{-2}$) would then be subsequently appropriate to identify the macroscopic, 3D current across the gap, since $\bar{\chi}$ is always unity for 3D coordinates [35].

Furthermore, Ref. [34] asserted that conformal mapping [36] cannot be used to solve for a potential $\phi$ that satisfies the Poisson's equation (i.e., $\nabla^2\phi \neq 0$). While the calculations with the Laplace's equation (i.e., of the form $\nabla^2\phi_0 = 0$) are a particular class of equations that are preserved [37], preservation of the differential equation is not a necessary condition for applying conformal mapping [38].

1-D Spherical SCLC

A. M. Darr[G], N. R. Sree Harsha[G], and **A. L. Garner**, "Response to Comment on "A coordinate system invariant formulation for space-charge limited current in vacuum" [APL 119, 206101 (2021)]," *Applied Physics Letters* **119**, 206102 (2021).

A second comment raised the following concerns [39] regarding our derivation of space-charge limited current (SCLC) using variational calculus (VC) [1]: (i) Unequal cathode and anode currents for nonplanar geometries; (ii) Maximum power leading to a minimum energy state as the proper implementation of VC; and (iii) Generalization to non-zero initial velocity leads to non-physical results. Song *et al*. also report particle-in-cell (PIC) simulation results purportedly supporting the Langmuir-Blodgett (LB) model [6] rather than VC [2]. PIC calculations of SCLC are challenging, even for apparently simple two-dimensional (2-D) planar geometries, motivating the development of improved SCLC algorithms [29]. Song *et al*. claim to provide the first spherical PIC simulations to demonstrate the validity of the LB solution (or at least the mathematical fit from Ref. [33]) [39]. Unfortunately, it is impossible to discern the validity or accuracy of these PIC results since Song *et al*. only describe the geometry and radial discretization, leaving several questions unanswered. How was the sensitivity of cold emission PIC simulations to algorithmic parameters (such as the precise initial location of injected electron in the mesh, or the method of injection) addressed? How did they track non-radial velocity, current components, and radial ray spreading (over the finite emission patch, each electron will travel along a different, diverging radial path)? How was symmetry implemented? What solid angle was chosen for emission? Since spherical surfaces are notoriously impossible to project onto 2-D, how was the inherently three-dimensional (3-D) nature of spheres preserved in these simulations? What criterion was used to determine SCLC (e.g., zero-electric field at the cathode or maximum stable current in the gap)? Once validated, these results could address multiple long-standing problems in 1-D PIC simulations of spherical SCLC, including the proximity of the cold emission infinite current density singularity at the cathode (a particular concern given the selection of low initial electron velocities, 0.001 to 0.1 eV [39]), sensitivity to initial parameters and algorithms, and non-$\hat{r}$ electron flow arising from a finite emission area. Because of the difficulties in 1-D spherical PIC simulations, an appropriate comparison of theory requires more details than can be provided in a Comment, so we look forward to seeing these details in a future full refereed journal article. Now, we focus on the three concerns listed above [40].

To the first concern, we agree that VC must be interpreted carefully with regards to dimensionality. The current equation $I = \oiint_S \vec{J} \cdot d\vec{S}$ described immediately above [30], as with the reflexively used $\nabla \cdot \vec{J} = 0$ continuity equation, assumes a 3-D space. However, directly interpreting our VC results requires applying the appropriate 1-D formalism to the divergence [30]. The divergence theorem states

$$\iiint_V (\nabla \cdot \vec{F}) \mathrm{d}V = \oiint_S (\vec{F} \cdot \hat{\mathrm{n}}) dS, \tag{18}$$

from which we may identify $\vec{F} = \bar{\chi}(\vec{x})\vec{J}$ [30], where $\bar{\chi} = 1, r, r^2$ for planar, cylindrical, and spherical geometries, respectively [35]. Thus,

$$I = \oiint_S \bar{\chi}(\vec{x})\vec{J} \cdot d\vec{S}. \tag{19}$$

As previously noted [29], VC gives spherical SCLC as $\vec{J} \propto r^{-4}$. Since $\bar{\chi}(\vec{r}) = r^2$ [35] and $d\vec{S} \propto r^2$ for spherical coordinates, the integrand in (19) is constant, making $I$ constant in the spherical diode. For cylindrical coordinates, $\vec{J} \propto r^{-2}$ [29], $\bar{\chi}(\vec{r}) = r$ [35], and $d\vec{S} \propto r$, making the integrand in (19) constant.

While current or power may be generally identified as the *extremum* of interest, SCLC is the limiting condition on an emitter that could produce functionally limitless current through, say, strong field emission. Thus, the proper starting comparison is not zero current, but rather nigh-infinite. Stating power in terms of gap voltage $V_G$ and current, $P = V_G I$, shows that the minimum, nontrivial (neither infinite nor zero) current clearly minimizes power. Furthermore, our planar VC result [29] recovers Child-Langmuir exactly, supporting our choice to extremize current; only in cases where multiple, nontrivial solutions exist will the maximum current be chosen, such as when initial velocity is nonzero. Equation (A5) of Ref. [39] selects the incorrect branch cut for the fourth root, leading to an incorrect sign – the correct choice [41] aligns our approach with Ref. [42], which is the bifurcation solution. Another adjustment to VC [41] avoids the bifurcation solution, which is a singularity, and returns the true SCLC for nonzero initial velocity numerically. Subsequently, we developed a correction for the true SCLC for a nonzero, nonrelativistic initial velocity for any geometry [43], that agrees with the accepted correction for Child-Langmuir in Cartesian coordinates [44]. We address this problem later in this report.

In conclusion, by carefully accounting for the 1-D nature of the VC derivation, clarifying the assumptions inherent in space-charge problems, and revealing errors in the derivation from Ref. [39], we have addressed all three concerns. VC exactly recovers the universally accepted planar SCLC, while offering fully analytic, flexible extensions to other common geometries. Ultimately, physical experiments must demonstrate which, if any, of the available SCLC theories and simulations accurately predict natural space-charge limited systems.

## Alternative Techniques for SCLC in 1-D Nonplanar Diodes

### Conformal Mapping

N. R. Sree Harsha[G] and **A. L. Garner**, "Applying Conformal Mapping to Derive Analytical Solutions of Space-Charge-Limited Current Density for Various Geometries," *IEEE Transactions on Electron Devices* **68**, 264-270 (2021).

While VC is powerful, it is limited to geometries where the Laplacian and gradient are readily obtained; however, more realistic diodes and slow wave structures may not be amenable to such analysis. Thus, in parallel with another AFOSR grant, we applied conformal mapping to derive the analytical solutions for SCLC for various complicated geometries exhibiting curvilinear flow [36]. We first replicated the exact solution of SCLC for concentric cylindrical electrodes from VC

by using conformal mapping to transform the space-charge limited electric potential from the Child-Langmuir (CL) law for Cartesian coordinates. We then derived SCLC in other geometries by using conformal transformations to either the planar or concentric cylinder solution. Because the SCLC calculated using such conformal mappings depends only on the CL law, this may permit future incorporation of relativistic or quantum corrections to determine the appropriate relationships for more complicated geometries.

We first consider a cathode and an anode as two concentric cylinders of infinite length with radii $R_C$ and $R_A$, respectively. The cross-sections of these cylinders can be represented in the complex *z*-plane by $z = Re^{i\theta}$. The transformation $w = f(z) = \ln z$ maps the circles into lines in the *w*-plane [45]. Applying the 1-D representation of $\phi$ to the *w*-plane yields

$$\phi = \frac{V(u - u_C)^{4/3}}{(u_A - u_C)^{4/3}}. \tag{20}$$

Transforming (20) into the *z*-plane gives the potential in the *z*-plane as

$$\phi = V\frac{(\ln R - \ln R_C)^{4/3}}{(\ln R_A - \ln R_C)^{4/3}} = V\left[\frac{\ln(R/R_C)}{\ln(R_A/R_C)}\right]^{4/3}. \tag{21}$$

Substituting (21) into Poisson's equation and applying the Laplacian in cylindrical coordinates yields the SCL current density near the cathode for cylindrical coordinates as

$$J_{\mathrm{SCL}} = \frac{4}{9}\epsilon_0\sqrt{\frac{2e}{m}}\frac{V^{3/2}}{R_C^2[\ln(R_A/R_C)]^2}, \tag{22}$$

which agrees with the result from VC [29]. Table I summarizes the results for other geometries considered.

TABLE VII.I: Summary of results using conformal mapping to calculus space-charge limited current [36].

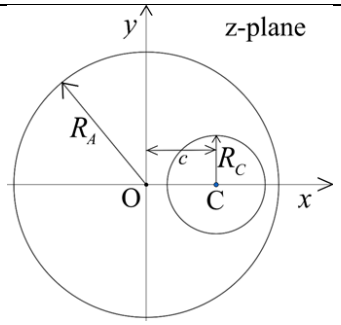


A cross-section of eccentric cylinders with anode of radius $R_A$ and cathode of radius $R_C$ and a displacement $c$ between their centers in the $z$-plane.

$$J_{\mathrm{SCL}} \approx \frac{4\epsilon_0}{9}\sqrt{\frac{2e}{m}}\frac{V^{\frac{3}{2}}}{R_C^2\left(\cosh^{-1}\frac{(R_A^2+R_C^2-c^2)}{2R_CR_A}\right)^2}.$$

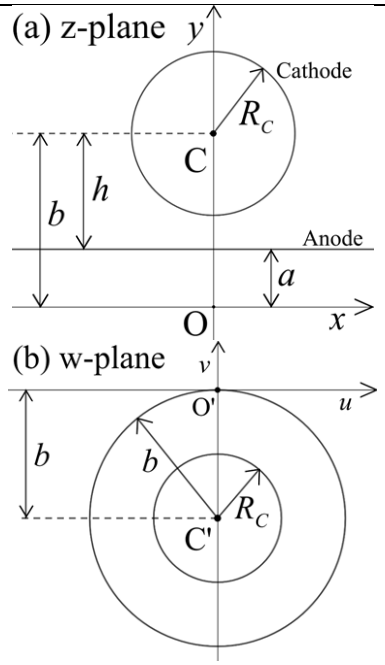


(a) A cross-section in $z$-plane of infinite plane as the anode placed at a distance $h$ from the center of the cylindrical cathode C of radius $R_C$ such that $R_C << h$. (b) The anode and the cathode are transformed into two concentric circles centered at C' in the $w$-plane.

$$J_{\mathrm{SCL}} \approx \frac{4\epsilon_0}{9}\sqrt{\frac{2e}{m}}\frac{V^{3/2}}{R_C^2\left(\ln\left[\left(h+\sqrt{h^2-R_C^2}\right)/R_C\right]\right)^2}$$

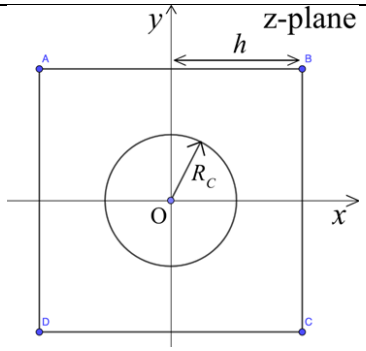


A cross-section of a doubly connected region consisting of a cylindrical cathode centered inside a square anode. The anode may be mapped onto an annulus using a numerical transformation approximation.

$$J_{\mathrm{SCL}} \approx \frac{4}{9}\epsilon_0\sqrt{\frac{2e}{m}}\frac{V^{3/2}}{R_C^2[\ln(1.08h/R_C)]^2}.$$

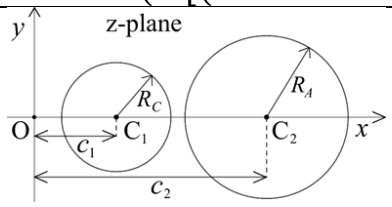


A cross-section of two external cylinders in the $z$-plane mapped onto an annulus centered at the origin in the $w$-plane by using fractional linear transformation.

$$J_{\mathrm{SCL}} \approx \frac{4\epsilon_0\sqrt{2e}}{9\sqrt{m}}\frac{V^{3/2}}{R_C^2\left(\ln\frac{R_A}{R_C}+\ln\frac{c_1+\sqrt{c_1^2-R_C^2}}{c_2+\sqrt{c_2^2-R_A^2}}\right)^2}$$

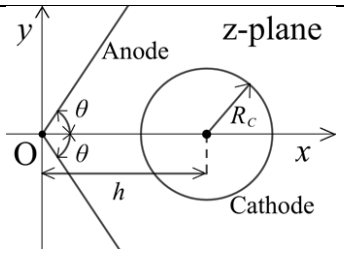


A cross-section of two 1-D planar anodes intersecting at an angle $2\theta$ at the origin and a cylindrical cathode of radius $R_C$ at a distance $h$ from the $y$-axis.

$$J_{\mathrm{SCL}} \approx \frac{16\theta^2\epsilon_0}{9\pi^2}\sqrt{\frac{2e}{m}}\frac{V^{3/2}}{R_C^2(\ln\left[2(h/R_C)^{2\theta/\pi}\right])^2}.$$

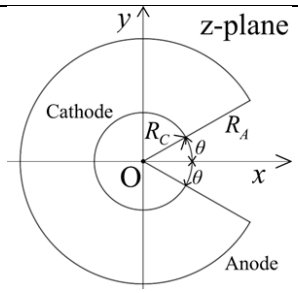


A cross-section of a concentric slotted diode consisting of a slotted anode of radius $R_A$, and an unslotted cathode of radius $R_C$, and a slot represented by angle $2\vartheta$.

$$J_{\mathrm{SCL}} \approx \frac{4}{9}\epsilon_0\sqrt{\frac{2e}{m}}\frac{V^{3/2}}{R_C^2(\ln\left[R_A/R_C\right])^2}$$

We also applied this technique to a tip-to-tip geometry by representing the cathode and the anode by hyperboloids in the prolate spheroidal coordinate system with $v_C \in (0, \pi/2)$ and $v_A \in (\pi/2, \pi)$ respectively [46]. We assumed symmetry in the azimuthal direction and considered 1-D analysis such that the SCLC potential $\phi$ was only a function of $v$. For boundary conditions of $\phi(v_C) = 0$, $\phi(v_A) = V_{\mathrm{g}}$, and $d\phi/dv|_{v=v_C} = 0$, we obtained

$$\phi = \frac{V_{\mathrm{g}}}{\eta^{4/3}}\left[\ln\left(\tan\frac{v}{2}\right) - \ln\left(\tan\frac{v_C}{2}\right)\right]^{4/3}. \tag{23}$$

where the sharpness of the tips employed in each geometry is quantified by the dimensionless parameter $\eta \equiv \ln(\tan(v_A/2)) - \ln(\tan(v_C/2))$. Combining (23) with (1) yields

$$J_{\mathrm{SCL}}^{\mathrm{t-t}} = \frac{\gamma}{a^2\sin^4 v_C}\frac{V_{\mathrm{g}}^{3/2}}{\eta^2}. \tag{24}$$

For a tip-plate geometry, where the cathode is represented by a sharp tip $v_C$ and the anode is represented by an infinite plane (i.e. $v_A \to \pi/2$), the SCLC is obtained by considering $v_A \to \pi/2$ to yield

$$J_{\mathrm{SCL}}^{\mathrm{t-p}} = \frac{\gamma}{a^2\sin^4 v_C}\frac{V_{\mathrm{g}}^{3/2}}{[\ln(\tan(v_C/2))]^2}. \tag{25}$$

With the distance between the apex of the tip and the plate represented by $D_0$ and radius of the cathode tip by $R_C$, the scaling factor can be written as $a^2 = D_0(D_0 + R_C)$ [47] and by defining $\beta = D_0/R_C = \cot^2 v_C$, which also gives $v_C = \tan^{-1}\left(1/\sqrt{\beta}\right)$ and $\sin^4 v_C = R_C^2(D_0 + R_C)^{-2}$, (13) may be written in terms of the CL law with $D = D_0$ as

$$\frac{J_{\mathrm{SCL}}^{\mathrm{t-p}}}{J_{\mathrm{CL}}} = \frac{\beta(1+\beta)}{\left[\ln\left(\sqrt{1+\beta}+\sqrt{\beta}\right)\right]^2}. \tag{26}$$

For $\beta \ll 1$, expanding (26) with $\beta = D_0/R_C$ gives

$$\frac{J_{\mathrm{SCL}}^{\mathrm{t-p}}}{J_{\mathrm{CL}}} \approx 1 + \frac{4\beta}{3} + \frac{4\beta^2}{15} = 1 + \frac{4D_0}{3R_C} + \frac{4D_0^2}{15R_C^2}. \tag{27}$$

For fixed $D_0$, we recover $J_{\mathrm{SCL}}^{\mathrm{t-p}} \to J_{\mathrm{CL}}$ as $R_C \to \infty$. When $\beta \gg 1$, (26) becomes

$$\frac{J_{\mathrm{SCL}}^{\mathrm{t-p}}}{J_{\mathrm{CL}}} \approx \frac{4\beta^2}{[\ln(4\beta)]^2} = \frac{(4\,D_0^2/R_C^2)}{[\ln(4\,D_0/R_C)]^2}. \tag{28}$$

Fig. 4 compares the exact solution for $J_{\mathrm{SCL}}^{\mathrm{t-p}}/J_{\mathrm{CL}}$ as a function of $\beta$ from (25) with the approximations from (26) and (27) to show that $J_{\mathrm{SCL}}^{\mathrm{t-p}}/J_{\mathrm{CL}} > 1$ and increases with increasing $\beta$ (or decreasing $v_C$); regression models show that $J_{\mathrm{SCL}}^{\mathrm{t-p}} \propto D_0^{-0.55}$ [48].

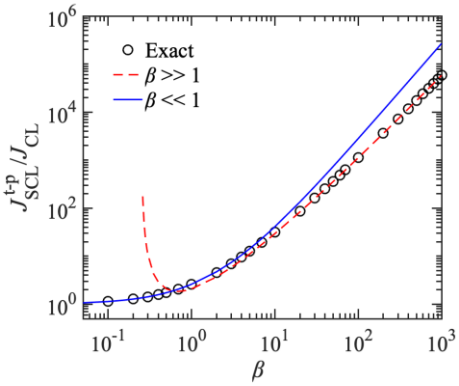


FIG. VII.4. The black circles show the normalized SCLC density $J_{\mathrm{SCL}}^{\mathrm{t-p}}/J_{\mathrm{CL}}$ as a function of $\beta = \cot^2 v_C$ given by (11), where $J_{\mathrm{SCL}}^{\mathrm{t-p}} \to J_{\mathrm{CL}}$ as $\beta \to 0$ or as $v_C \to \pi/2$. The blue solid and red dashed curves show the approximations for $\beta \ll 1$ given by (27) and $\beta \gg 1$ given by (28), respectively.

Lie Point Symmetries

N. R. Sree Harsha[G], J. M. Halpern[U], A. M. Darr[G], and **A. L. Garner**, "Space-charge-limited current density for nonplanar diodes with monoenergetic emission using Lie-point symmetries," *Physical Review E* **106**, L063201 (2022).

Consider the general first-order ODE of the form

$$\frac{dy}{dx} = f(x,y), \tag{29}$$

where $f(x,y)$ is a smooth function of $x$ and $y$. If the function $f$ in (29) is a function of $x$ alone (i.e., $f(x,y) \equiv f(x)$), we can readily solve (1) by carrying out the quadrature

$$y = \int f(x)dx + c, \tag{30}$$

for some integration constant $c$. If, however, $f(x,y)$ in (29) cannot be separated into a product of two functions such that $f(x,y) = g(x)h(y)$ for some smooth functions $g$ and $h$, the solution to the ODE cannot be obtained directly by carrying out a quadrature. For such situations, we can use the Lie-point symmetries of (29) to identify a set of canonical coordinates that reduces (29) to a form that can be solved directly by carrying out the quadrature (30) [49-51]. These canonical coordinates represent local transformations that map every solution set of a system to another solution set of the same system for which known solutions exist or can be obtained directly by taking the quadrature.

For an electron emitted from a cathode with initial velocity $v_0$, conservation of energy gives

$$v_p = v_0\sqrt{1 + \frac{2e\phi_p}{mv_0^2}}, \tag{31}$$

$$J_p = \epsilon_0 v_0 \frac{d^2\phi_p}{dx^2}\sqrt{1 + \frac{2e\phi_p}{mv_0^2}}. \tag{32}$$

The SCLCD at the cathode, $J_{\mathrm{SCL}}$, is given by

$$J_{\mathrm{SCL}} = \lim_{x\to x_C}[\max(J)] = \max\left[\lim_{x\to x_C}(J)\right], \tag{33}$$

where we define max() as a continuous functional that takes the expression on the right-hand side of (32) as an input and generates the maximum value of $J$ (denoted as $J_{\mathrm{SCL}}$) as the output. We have derived this for general geometries elsewhere. In canonical coordinates, we obtain

$$J_{\mathrm{SCL}} = \frac{\gamma V_{\mathrm{g}}^{3/2}}{(\zeta_A - \zeta_C)^2}\left(\beta + \sqrt{1+\beta^2}\right)^3, \tag{34}$$

where $\gamma = 4\epsilon_0\sqrt{2e/m}/9$, $\epsilon_0$ is the permittivity of vacuum, $e$ and $m$ are the charge and mass of the electron, respectively, $\beta^2 = 2^{-1}mv_0^2e^{-1}V_g^{-1}$, and $\zeta_C$ and $\zeta_A$ represent the locations of the cathode and anode in canonical coordinates, respectively.

We further show that the ratio between $J_{SCL}$ with nonzero $v_0$ may be related to its zero $v_0$ for any orthogonal geometry as

$$\frac{J_{\mathrm{q,SCL}}}{J_{\mathrm{q,SCL,0}}} = \left(\beta + \sqrt{1+\beta^2}\right)^3, \tag{35}$$

where $J_{\mathrm{q,SCL,0}}$ is the SCLCD with $v_0 = 0$ (i.e., $\beta = 0$). For $\beta \ll 1$, we approximate (35) as

$$\frac{J_{\mathrm{q,SCL}}}{J_{\mathrm{q,SCL,0}}} \approx 1 + 3\beta. \tag{36}$$

For $\beta \gg 1$, we approximate (35) as

$$\frac{J_{\mathrm{q,SCL}}}{J_{\mathrm{q,SCL,0}}} \approx 8\beta^3. \tag{37}$$

Figure 5 shows $J_{\mathrm{q,SCL}}/J_{\mathrm{q,SCL,0}}$ as a function of $\beta$ for the exact (35) and asymptotic [(36), (37)] solutions. Figure 6 shows $J_{\mathrm{c,SCL}}$ as a function of the canonical gap size $\delta_c = r_C^2[\ln(r_C/r_A)]^2$ for various $\beta$, which is true for any geometry.

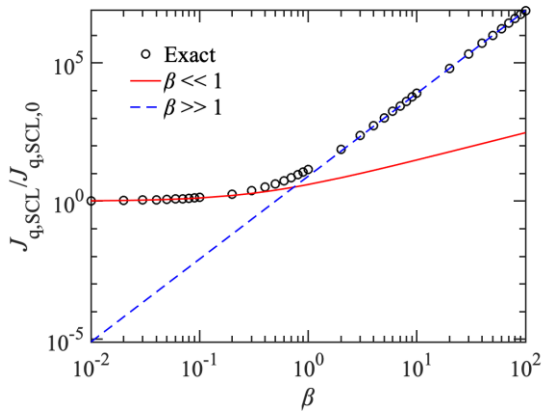


FIG. VII.5. The exact solution of the ratio of SCLCD in general coordinates to the corresponding SCLCD with zero injection velocity in general coordinates as a function of $\beta$ from (28) with limits for $\beta \ll 1$ from (30) and

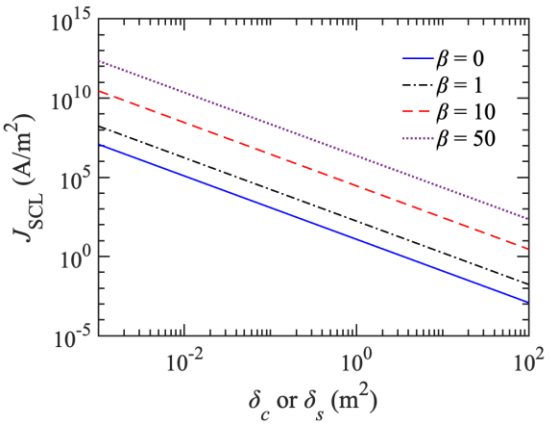


FIG. VII.6. SCLCD ($J_{\mathrm{SCL}}$) as a function of canonical gap size $\delta_c = r_C^2[\ln(r_C/r_A)]^2$ or $\delta_s = r_C^2[r_A - r_C]^2/r_A^2$ for cylindrical or spherical coordinates, respectively, for various $\beta$. The applied voltage is $V_{\mathrm{g}} = 30$ kV. Note that $J_{\mathrm{SCL}}$ is the same for any geometry for a given canonical

In summary, we have demonstrated how to obtain canonical coordinates to make Poisson's equation separable to solve for SCLCD in general orthogonal coordinates for nonzero monoenergetic injections velocities and then for four simple geometries. Of particular note, we have provided independent validation of previous calculations of SCLCD using VC for spherical, tip-to-tip, and tip-to-plate geometries. We have also shown that the correction factor to account for initial velocity for any coordinate system is independent of geometry, so it is straightforward to write SCLCD for monoenergetic emission for a known 1-D SCLCD with zero injection velocity. This may be valuable for complicated geometries that may not be amendable to this analysis, such as those we have studied previously using CM [36]. We have also demonstrated that 1-D SCLCD is independent of geometry once written as a function of canonical gap size (cf. Fig. 6); therefore, one may obtain SCLCD for a given geometry by applying the appropriate metric to the universal SCLCD. For ODEs and PDEs with nonobvious canonical coordinates, one may use Lie-point symmetries to derive the corresponding canonical coordinates

to simplify the ODEs and PDEs [52, 53]. This method provides various potential directions for future research. For instance, Lie-point symmetries may simplify the governing PDEs in cylindrical crossed-field diode geometries [54].

## Multidimensional Child-Langmuir for General Geometries

**[FEATURED]** N. R. Sree Harsha[G], M. Pearlman[P], J. Browning, and **A. L. Garner**, "A multi-dimensional Child-Langmuir law for any diode geometry," *Physics of Plasmas* **28**, 122103 (2021).

While prior theoretical studies of multi-dimensional space-charge-limited current (SCLC) assumed emission from a small patch in infinite electrodes [12,13], none have considered the more practical geometry in which the size of the emission area is on the same order of magnitude as the emitter. We apply variational calculus (VC) and conformal mapping, which have previously been used to derive analytic solutions for SCLC for non-planar geometries, to obtain mathematical relationships for general, multi-dimensional geometries [55]. We first derive a mathematical relationship between space-charge-limited potential and vacuum potential for a general diode and derive SCLC density for an eccentric spherical diode. We then apply VC and the Schwartz-Christoffel transformation to derive an exact analytic solution for a generalized two-dimensional planar geometry that reduces to the prior finite emitting patch for infinite electrodes to first order approximation. After generalizing this approach to determine SCLC density for any orthogonal diode by using the vacuum capacitance, we present an accurate analytical formulation of three-dimensional (3-D) CL law for parallel plate diodes with rectangular and disk geometries. These results demonstrate the utility for calculating SCLC for any geometry to guide experiment and simulation development.

Defining the dimensionless quantity $\bar{\phi} = \phi/V_g$ gives the potential in a space-charge limited diode with any geometry as

$$\overline{\phi_{SCL}} = \overline{\phi_0}^{\,4/3}, \tag{38}$$

such that the spatial profile of the electric potential of a space-charge-limited diode may be calculated directly from the vacuum potential with the 4/3-power dependence independent of geometry. Since $\phi_{SCL}$ satisfies the Poisson's equation with $\rho_{SCL}$ as the volumetric space charge density, given by $\nabla^2\phi_{SCL} = \rho_{SCL}/\epsilon_0$, the analytic solution of $\phi_{SCL}$for many diode geometries is not always possible [56]; however, the vacuum potential distribution can be easily obtained by solving the Laplace equation, given by $\nabla^2\phi_0 = 0$. Equation (38) thus provides an easy way to determine $\phi_{SCL}$ from $\phi_0$ for *any* geometry and determine $J_{SCL}$, as illustrated in the next section.

We now use the relationship between the space-charge-limited potential and the vacuum potential to formulate SCLC density in terms of the vacuum capacitance for a 2-D planar geometry with finite electrodes. Combining Poisson's equation and the electron force law gives the SCLC density for any diode geometry as

$$J_{\mathrm{SCL}} = \frac{\epsilon_0}{4}\sqrt{\frac{2e}{m_e}}\frac{|\nabla\phi_{\mathrm{SCL}}|^2}{\sqrt{\phi_{\mathrm{SCL}}}}. \tag{39}$$

Applying $\overline{\phi_{\mathrm{SCL}}} = \phi_{\mathrm{SCL}}/V_{\mathrm{g}}$, we can recast (39) as

$$J_{\mathrm{SCL}} = \frac{\epsilon_0 {V_{\mathrm{g}}}^{3/2}}{4}\sqrt{\frac{2e}{m_e}}\frac{\left|\nabla\overline{\phi_{\mathrm{SCL}}}\right|^2}{\overline{\phi_{\mathrm{SCL}}}^{1/2}}. \tag{40}$$

Combining (38) and (40) yields

$$J_{\mathrm{SCL}} = \frac{\epsilon_0 {V_{\mathrm{g}}}^{3/2}}{4}\sqrt{\frac{2e}{m_e}}\frac{\left|\nabla\overline{\phi_0}^{4/3}\right|^2}{\overline{\phi_0}^{2/3}}. \tag{41}$$

We also have

$$\left|\nabla\overline{\phi_0}^{4/3}\right|^2 = \frac{16\overline{\phi_0}^{2/3}}{9}\sum_{i=1}^{3}\frac{1}{h_i^2}\left(\frac{\partial\overline{\phi_0}}{\partial q_i}\right)^2 = \frac{16\overline{\phi_0}^{2/3}}{9}\left|\nabla\overline{\phi_0}\right|^2, \tag{42}$$

which we can combine with (41) to obtain the relationship between the SCLC density and the vacuum electric field as

$$J_{\mathrm{SCL}} = \frac{4\epsilon}{9}\sqrt{\frac{2e}{m_e}}{V_{\mathrm{g}}}^{3/2}\left|\nabla\overline{\phi_0}\right|^2. \tag{43}$$

We shall now consider an infinite parallel plate geometry where the anode and the cathode are infinite planes separated by a distance $D$ with the anode held at $\phi(D) = V_{\mathrm{g}}$ and the cathode held at $\phi(0) = 0$. Since $J_{1\mathrm{D}}$ represents the steady state current density, $J_{\mathrm{SCL}}$ near the cathode for this parallel plate geometry can be derived by taking volume average of (43). Defining $V$ as the total volume in the diode gap and $dV = dxdydz$ as the infinitesimal volume allows us to rewrite (43) as

$$J_{\mathrm{SCL}} = \frac{4\epsilon_0}{9}\sqrt{\frac{2e}{m_e}}V_{\mathrm{g}}^{3/2}\frac{\int_0^V\left|\nabla\overline{\phi_0}\right|^2 dV}{\int_0^V dV}. \tag{44}$$

Since the system's vacuum capacitance is given by $C_0 = \epsilon_0\int_0^V\left|\nabla\overline{\phi_0}\right|^2 dV$ [57], we can write (44) as

$$J_{\mathrm{SCL}} = \frac{4}{9}\sqrt{\frac{2e}{m_e}}V_{\mathrm{g}}^{3/2}\frac{C_0}{\int_0^V dV}. \tag{45}$$

Substituting the vacuum capacitance for this 1-D diode, given by $C_0 = \epsilon_0 WL/D$, in (45) and noting that the total volume is $\int_0^V dV = WLD$ recovers the familiar 1-D CL law.

For the 2-D CL law, we consider a pair of parallel planes of length *W*, separated by a distance *D*, which field lines as shown in Fig. 7. Note that these planes are finite in the direction of length (the *x*-axis) and infinite in depth (the *y*-axis). Palmer applied the Schwartz-Christoffel transformation to determine the vacuum capacitance, including all the effects of the fringing fields, of such a system [58]. Assuming modulus $m \in (0,1)$ and a corresponding complementary modulus $\mu \equiv \sqrt{1-m^2}$, allows the construction of an argument $\omega$ using

$$\sin^2\omega = \frac{F\left(\frac{\pi}{2},\mu\right) - E\left(\frac{\pi}{2},\mu\right)}{\mu^2 F\left(\frac{\pi}{2},\mu\right)}, \tag{46}$$

where $F(\pi/2,\mu)$ and $E(\pi/2,\mu)$ are the complete elliptic integrals of first and second kind with $F(\theta,\mu) = \int_0^\theta dt/\sqrt{1-\mu^2\sin^2 t}$ and $E(\theta,\mu) = \int_0^\theta \sqrt{1-\mu^2\sin^2 t}\,dt$ as the incomplete elliptic integrals of the first and second kind, respectively [59]. The values $m$, $\mu$ and $\omega$ are then used to obtain the ratio of $W/D$ using

$$\frac{W}{D} = \frac{F\left(\frac{\pi}{2},\mu\right)E(\omega,\mu) - E\left(\frac{\pi}{2},\mu\right)F(\omega,\mu)}{\left[E\left(\frac{\pi}{2},\mu\right) - F\left(\frac{\pi}{2},\mu\right)\right]F\left(\frac{\pi}{2},m\right) + F\left(\frac{\pi}{2},\mu\right)E\left(\frac{\pi}{2},m\right)}. \tag{47}$$

The capacitance per unit length corresponding to $W/D$ from (46) is given by $C_0^{(2\mathrm{D})} = \epsilon_0 F(\pi/2,\mu)/F(\pi/2,m)$ [56]. Hence, from (45), the average SCLC density is given by

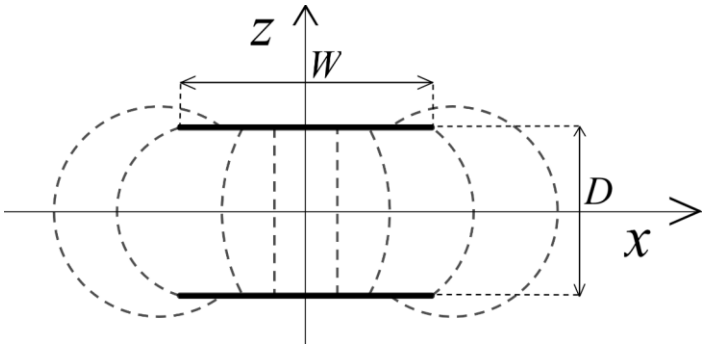


FIG. 7. The cross-section of the diode geometry for the 2-D CL law shown in *x*-*z* plane. A few of the fringing fields from the anode, positioned at $z = D/2$, to the cathode at $z = -D/2$ are approximately shown by longer dashed lines.

$$J_{2D} = \frac{4}{9}\sqrt{\frac{2e}{m_e}}V_g^{3/2}\frac{\epsilon_0 F\left(\frac{\pi}{2},\mu\right)}{WDF\left(\frac{\pi}{2},m\right)}. \tag{48}$$

Taking the ratio of (48) to the 1-D CL law gives the 2-D CL law as

$$\frac{J_{2D}}{J_{1D}} = \frac{F\left(\frac{\pi}{2},\mu\right)/F\left(\frac{\pi}{2},m\right)}{W/D}. \tag{49}$$

Since the SCLC density for a 2-D planar diode is independent of $z$ in Fig. 17, (49) also represents the current density at the cathode [60]. Furthermore, (49) may be used to find the exact SCLC density for a 2-D diode by numerically solving for the complete elliptic integrals.

In addition to the exact solution to (29), we may make two approximations to derive approximate closed form solutions. For $W/D \gg 1$, we can use Love's approximation [58], to write (49) to the first order of $W/D$ as

$$\frac{J_{2D}}{J_{1D}} \approx 1 + \frac{1}{\pi\left(\frac{W}{D}\right)} + \frac{\ln\left(\frac{2\pi W}{D}\right)}{\pi\left(\frac{W}{D}\right)}. \tag{50}$$

From (50), $J_{2D}/J_{1D} \to 1$ as $W/D \to \infty$. While the first two terms on the right-hand side of (50) exactly match the 2-D Child-Langmuir solution for emission from a finite emission area along an infinite electrode [100], the third term accounts for the additional contribution of fringing fields for emission from a finite electrode. For $W/D \ll 1$, (49) can be approximated as [58]

$$\frac{J_{2D}}{J_{1D}} \approx \frac{\pi}{\left(\frac{W}{D}\right)\ln\left(\frac{4D}{W}\right)} \tag{51}$$

Figure 8 compares the exact 2-D CL law and the approximations for large and small values of $W/D$. For $W/D < 0.5$, (51) is a very good fit to the exact solution from (49); for $W/D > 2$, (50) agrees well with (49). We have also extended this to 3-D to obtain

$$\frac{J_{3D}}{J_{1D}} \approx \frac{F\left(\frac{\pi}{2},\mu_1\right)/F\left(\frac{\pi}{2},m_1\right)}{W/D} + \frac{F\left(\frac{\pi}{2},\mu_2\right)/F\left(\frac{\pi}{2},m_2\right)}{L/D} - 1 \tag{52}$$

when $W$ and $L$ are comparable to $D$.

## Application of Variational Calculus to a Crossed-Field Diode

A. M. Darr[G], R. Bhattacharya[P], J. Browning, and **A. L. Garner**, "Space-Charge Limited Current in Planar and Cylindrical Crossed-Field Diodes using Variational Calculus," *Physics of Plasmas* **28**, 082110 (2021).

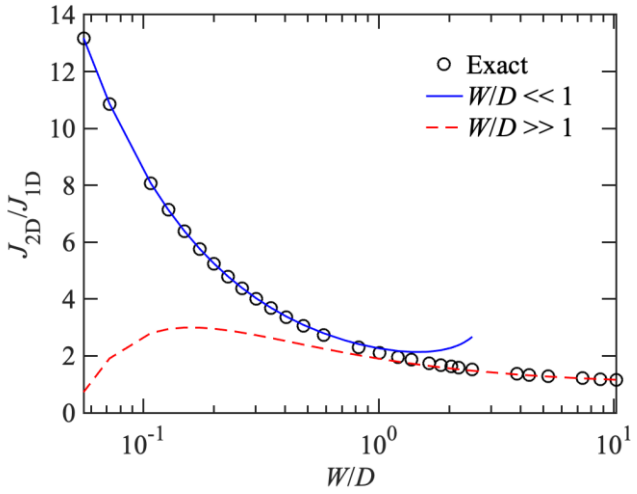


FIG. VII.8. A semi-log plot of 2-D space-charge limited current $J_{2D}$ normalized to 1-D space-charge-limited current $J_{1D}$ as a function of log($W/D$) for the exact 2-D CL law obtained from (25) and approximations for $W/D$>>1 given by (26) and $W/D$<<1 given by (27) are plotted against $W/D$.

The formalisms of variational calculus require a physical quantity to be maximized or minimized; as in the case with $B = 0$, this means extremizing $P = VI$ with power $P$ and emitted current $I$ from an emission area $A$ such that $I = \int JA$ [10] For a crossed-field diode, the individual components of current follow continuity, but the total magnitude $|\vec{J}|$ is not constant across the gap due to stored binormal current. In planar and cylindrical geometries, we use the binormal velocities to obtain

$$J_p = \epsilon_0 \phi_{xx} \left[\frac{2e\phi}{m} - \Omega^2 x^2\right]^{1/2} \tag{53a}$$

$$J_c = \epsilon_0 \left(\phi_{rr} + \frac{1}{r}\phi_r\right)\left[\frac{2e\phi}{m} - \left(\frac{\Omega r}{2}\right)^2\left(1 - \frac{R_c^2}{r^2}\right)^2\right]^{1/2}, \tag{53b}$$

for planar and cylindrical, respectively where we have dropped the vector notation since current and velocity are co-directional and use coordinate subscripts ($x$, $r$, and, later, generalized coordinate $q$) to denote partial derivatives.

Since voltage is fixed,

$$I_p = \int J_p A \propto \int \phi_{xx}\left[\frac{2e\phi}{m} - \Omega^2 x^2\right]^{1/2}, \tag{54}$$

for planar geometry and

$$I_c = \int J_c A \propto \int (r\phi_{rr} + \phi_r)\left[\frac{2e\phi}{m} - \left(\frac{\Omega r}{2}\right)^2\left(1 - \frac{R_c^2}{r^2}\right)^2\right]^{1/2}. \tag{55}$$

for cylindrical geometry. Equations (54) and (55) may be transformed to the Euler-Lagrange form [31]; to ease expression, we use dimensionless variables: $\bar{x} = x/D$, $\bar{r} = r/R_a$, $\bar{B} = B/B_H$, $\bar{\phi} = \phi/V$, $\bar{J} = J/J_{SCLC}$, with space-charge limited current (SCLC) $J_{SCLC}$ denoting the $B = 0$ solution for the given geometry; note this means $\bar{R}_c = \bar{a}$, $\bar{R}_a = 1$ for any cylindrical geometry. We can then obtain

$$\nabla^2\bar{\phi} = \frac{\bar{\phi}_{\bar{x}}^2 - 4\bar{B}^2\bar{\phi}_{\bar{x}}\bar{x} + 4\bar{B}^2\bar{\phi}}{4\bar{\phi} - 4\bar{B}^2\bar{x}^2}, \tag{56}$$

for planar geometry and

$$\nabla^2\bar{\phi} = \frac{\bar{\phi}_{\bar{r}}^2 - \frac{4\bar{B}^2\bar{r}\bar{\phi}_{\bar{r}}}{(1-\bar{a}^2)^2}\left[\frac{\bar{r}^4-\bar{a}^4}{\bar{r}^4}\right] + \frac{8\bar{B}^2\bar{\phi}}{(1-\bar{a}^2)^2}\left[\frac{\bar{r}^4+\bar{a}^4}{\bar{r}^4}\right] - \left(\frac{2\bar{B}\bar{r}}{(1-\bar{a}^2)^2}\right)^2\left[\frac{\bar{r}^2-\bar{a}^2}{\bar{r}^2}\right]^4}{4\bar{\phi} - \frac{4\bar{B}^2\bar{r}^2}{(1-\bar{a}^2)^2}\left[\frac{\bar{r}^2-\bar{a}^2}{\bar{r}^2}\right]^2} \quad (57)$$

for cylindrical geometry. Equations (56) and (57) are highly nonlinear; the additional magnetic terms prevent an exact analytic solution. Furthermore, (56) and (57) can become numerically unstable as $\bar{B} \to 1$ due to the singularity at $\bar{B} = 1$.

Figure 9 shows that the full results from the variational approach (56) match exactly with existing models for planar crossed-field diodes [61,62], and the near-planar cylindrical ($\bar{a} = 1.3^{\pm 1}$) solution (57) matches almost as closely, as expected from experiments [63-66]. One limitation of the numerical solutions of (57) is a failure to converge for $0.95 \lesssim \bar{B} \lesssim 1.05$ due to the singularity at $\bar{B} = 1$, especially for $\bar{a}$ far from unity (highly cylindrical). Because of the agreement between near-planar cylindrical and planar geometries from (56) and (57), respectively, the prior 1-D planar theory [61,62] is recommended for practical calculations since (56) is not closed form. Since (56) and (57) match existing theory [61,62] at appropriate limits, they represent analytic, first-principles models for crossed-field SCLE in planar and more common cylindrical geometries. Examining Fig. 9 more closely, the choice of normalizing $J_{cr}$ to $J_{SCLC}$ means inverse and conventional magnetron geometries return the same result; that is, $\bar{R}_c$ and $\bar{R}_a$ may be interchanged, hence the single curve for $\bar{a}^{\pm 1}$. When transformed to physical units, the SCLC normalizations will yield different physical values for conventional and inverted devices. Figure 9 makes the overall trend clear: increasingly cylindrical ($\bar{a}$ far from unity) diodes experience increasingly extreme deviations from $J_{SCLC}$, especially as $\bar{B} \to 1^-$.

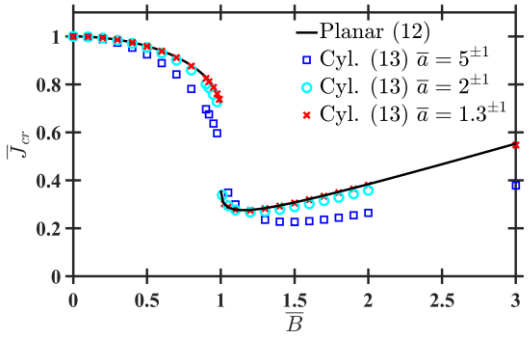


FIG. VII.9. Dimensionless current density $\bar{J}_{cr}$ as a function of dimensionless magnetic field $\bar{B}$, where the solid line represents the planar analytic solution (12), and the points represent solutions to (13) for cylindrical geometries with various ratios of cathode ($R_c$) -to-anode ($R_a$) radius $\bar{a} = R_c/R_a$. Due to the normalization of $\bar{J}$, the cylindrical results are identical for both conventional ($\bar{a}$) and inverted ($\bar{a}^{-1}$) magnetron geometries, that is for $\bar{a}$ and $\bar{a}^{-1}$, expressed as $\bar{a}^{\pm 1}$, since the cathode and anode may be interchanged. The cylindrical calculations are numerically unstable for $0.95 \lesssim \bar{B} \lesssim 1.05$.

Although (12) matches expected theoretical results [61,62], it is important to acknowledge that neither this new variational model nor any of the accepted planar crossed-field models from the literature [61,62,67-69] explain many experimental results clearly showing $\bar{J}_{cr} \to 0$ as $\bar{B} \to 1^-$ [64-66,70]. While Fig. 9 shows these trends may occur for highly cylindrical diodes, all the experiments were for near-planar geometries with $\bar{a} \approx 1$; none of the experiments exceeded $\bar{a} = 1.3^{\pm 1}$. At the time, these experimental results were hypothesized, variously, to be the result of weak relativistic effects, inhomogeneities or misalignments in the experimental setup, or

secondary emission [64-66,70]. Given the common trend among experiments with widely differing characteristics over an order of magnitude in voltage, both inverse and conventional configurations, many different gap distances, and two different research groups performing the experiments – it is unlikely that any one factor caused the trend. In fact, given that these represent the bulk of all experimental results for crossed-field SCLE for $\bar{B} < 1$, it may be possible these results are universal.

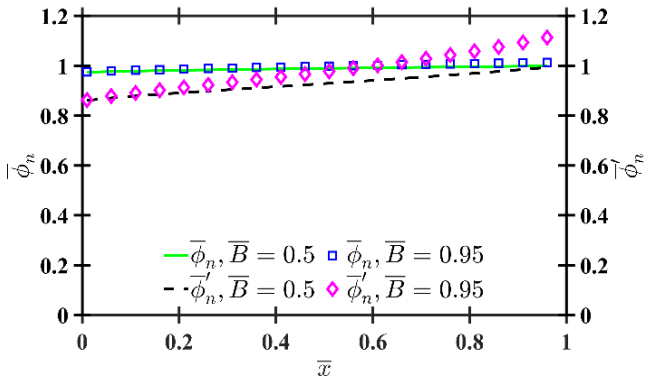


FIG. VII.10. Ratio of the dimensionless electric potential $\bar{\phi}$ from (12) for dimensionless magnetic fields $\bar{B}$ to the dimensionless electric potential in a non-magnetic planar space-charge limited gap $\bar{\phi}_{CL}$ [29], given by $\bar{\phi}_n \equiv \bar{\phi}/\bar{\phi}_{CL}$, and the ratio of the normalized electric field magnitudes for magnetic and non-magnetic gaps, given by $\bar{\phi}_n' \equiv (d\bar{\phi}/d\bar{x})\,/(d\bar{\phi}_{CL}/d\bar{x})$, as functions of $\bar{x}$ from 0 (cathode) to 1 (anode).

Considering Fig. 9, $\bar{J}_{cr} < 1$ for all $0 < \bar{B} < 1$. From the energy balance and the velocity, we also know the exact cathode-to-anode and binormal velocities at the anode. Since the total current – including stored current – cannot effectively exceed $J_{SCLC}$ without violating the space-charge limited condition, we may estimate $\left|\vec{J}\right|_{anode} = J_{SCLC}$ and compare normal and binormal velocities to determine normal (collected) anode current density. Since $\vec{J}$ obeys three-dimensional continuity, $\nabla \cdot \vec{J} = 0$ over the bulk diode (as opposed to local continuity), the normal current density at the anode may be recalculated as cathode emission current

$$\bar{J}_{cr} = \sqrt{1 - \bar{B}^2}. \tag{58}$$

Equation (58), unlike (56), accounts for bulk, three-dimensional effects in the entire diode explicitly, and matches phenomenologically-based fits precisely [70]. This simple model must be used cautiously, however, as there is no guarantee that $\left|\vec{J}\right|_{anode} = J_{SCLC}$. Alternatively, we may begin by noting the similarities shown in Fig. 10 between $\bar{\phi}(\bar{x})$ from the solution of (56) and SCLC [29]. We may then compute the total average current $\langle\left|\vec{J}\right|\rangle$ in a planar gap assuming the potential profile follows the SCLC limit (CL in planar), noting $J_y/J_x = v_y/v_x$, using appropriate relationships for the velocities, and assuming $\bar{\phi}(\bar{x}) = \bar{x}^{4/3}$ as in CL yields a limit for planar emission current $J_x$ as

$$\bar{J}_x = \frac{2}{3}\bar{J}_{CL}\frac{\bar{B}^3}{\sin^{-1}(\bar{B}) - \bar{B}\sqrt{1-\bar{B}^2}}, \tag{59}$$

which has the limit $\bar{J}_x \to (4\bar{J}_{CL})/(3\pi)$ as $\bar{B} \to 1^-$ and $\bar{J}_{cr} \to \bar{J}_{CL}$ as $\bar{B} \to 0$. Equation (59) is more restricted than the full solution (56); Fig. 10 shows that the CL potential is larger, resulting in a smaller prediction than expected in (59).

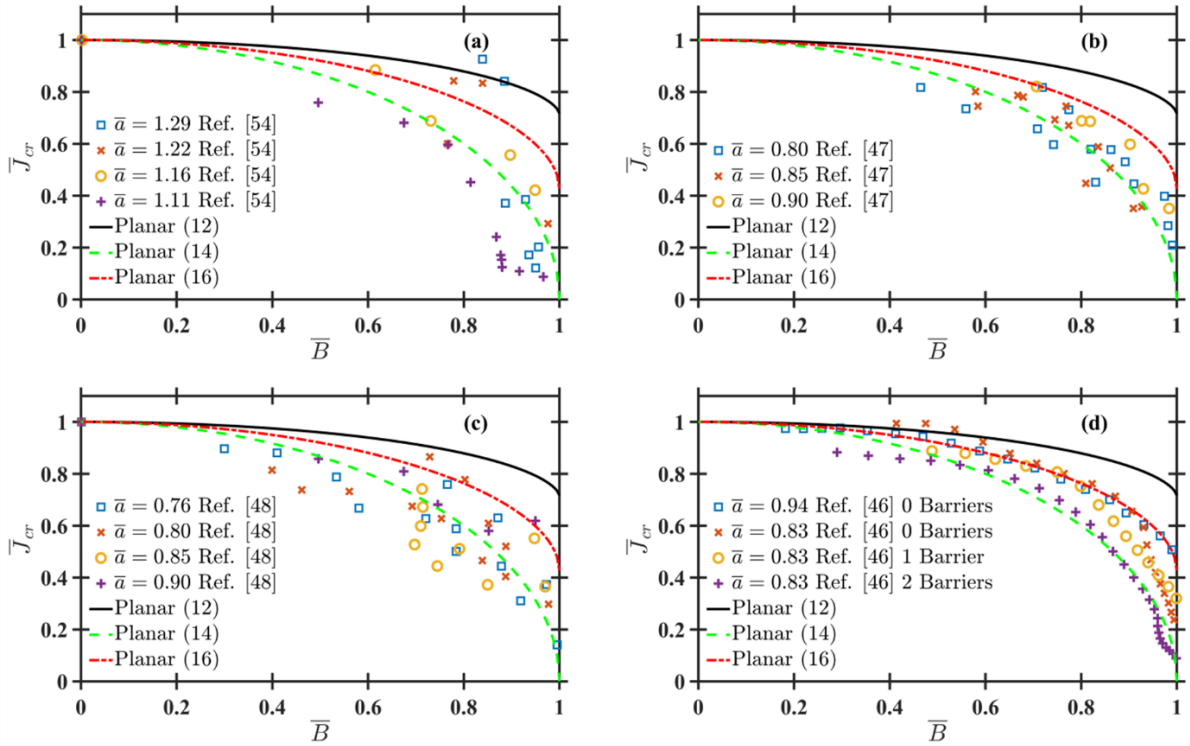


FIG. VII.11. Dimensionless current density $\bar{J}_{cr}$ as a function of dimensionless magnetic field $\bar{B}$. The data points in (a)-(d) are experimental data from Refs. [66], [64], [65], and [63] ([54], [47], [48], and [46], respectively, in the figure), respectively, where $\bar{a} = R_c/R_a$ is the ratio of the cathode-to-anode radii. The electron barriers in (d) are end-hats to prevent leakage current, similar to those depicted in Fig. 1. Since $\bar{a} \approx 1$ (near-planar), the experiments are compared to theoretical results from 56 [(12) in the figure], 58 [(14) in the figure], and (59) [(16) in the figure]. The cylindrical calculations are numerically unstable for approximately $\bar{B} > 0.95$.

While the simple analytic solutions from (58) and (59) are limited by their respective constituent assumptions, they capture enough of the physics to adequately model experimental results. Comparing these and the full theory from (56) we omit (57) since the most extreme experimental $\bar{a}$ falls within $1.3^{\pm 1}$ [64-66,70], which we showed in Fig. 9 to match planar nearly perfectly) to normalized experimental data, Fig. 11 shows the full theory cannot adequately model experimental results, while the simple theories, especially (58), can. All experiments are normalized to reported data for $\bar{B} = 0$ (since some papers did not report dimensional data, we assume near-planar $B_H$ when normalizing). The panels of Fig. 11 are ordered chronologically; a trend toward cleaner data is observed in later experiments. Figs. 11(a)-(c) show that experiments conducted in the 1970s [64-66] agree well with the simple models, especially (58), which was noted phenomenologically at the time without any formal or first-principles derivation [71]. Later experiments summarized in Fig. 4(d) include data [42] collected after the derivation of the 1D model [61,62]. In addition to reporting cleaner data, the data in Fig. 11(d) also exhibits two distinct modes following (58) or (59), but, notably, never (56). The "barriers" are end-hats at one or both axial ends of the

cylindrical diode, which prevent current leakage and make the data closer to the theoretical limit. As expected, the data with barriers, which corresponds to the condition with the minimum current leakage or maximum current stored in the gap, matches most closely with (58).

The 1D theory was validated by the 1-D spatial and 3-D velocity (1d3v) particle-in-cell (PIC) code XPDP1 [62,72-76]. The agreement between simulation and theory and the disagreement with experimental results indicate that the theory and simulations do not adequately represent the physical reality of the four crossed-field experimental diodes considered [64-66,70]. The variational calculus extension to cylindrical geometry (13) has not improved predictions enough; to investigate this further, we conducted fully three dimensional (3D) simulations of both planar and cylindrical diodes described in Section II.B.

Figure 12 shows that our simulations agree much better with experiment for $\overline{B} < 1$, while validating planar theory (56) [62] for $\overline{B} > 1$. This motivates a much more careful study and design of experimental crossed-field diodes, especially those operating at $\overline{B} < 1$.

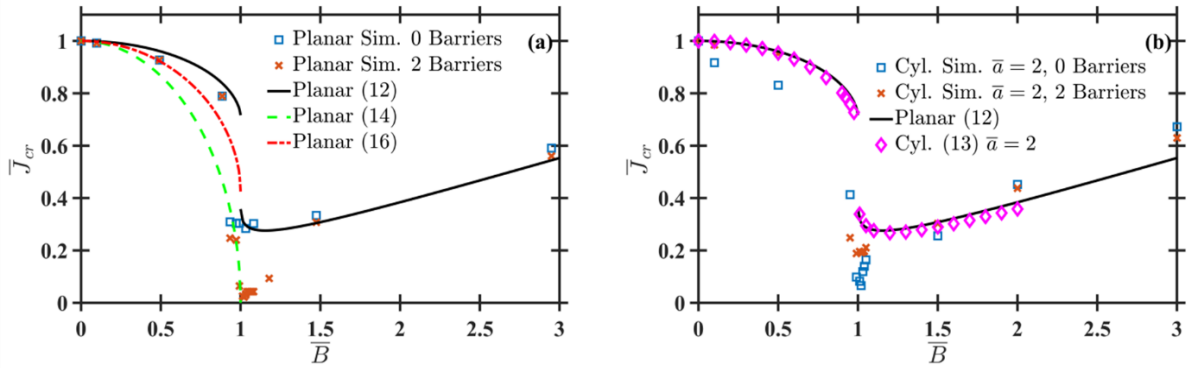


FIG. VII.12 Dimensionless current density $\bar{J}_{cr}$ as a function of dimensionless magnetic field $\bar{B}$. The data points in (a) and (b) are CST Particle Studio simulation results for planar and cylindrical geometries, respectively, where $\bar{a} = R_c/R_a$ is the ratio of the cathode-to-anode radii. The barriers are the end-hats shown in Fig. 1. (a) Comparison of planar simulations with no or two barriers to planar theory from (56), (58), and (59). (b) Comparison of cylindrical simulations with $\bar{a} = 2$ and either no or two end-hats to planar theory from (56) or cylindrical theory from (57). The cylindrical theory calculations are numerically unstable for approximately $0.95 \lesssim \bar{B} \lesssim 1.05$.

We hypothesize that the failure of (56), (57) and existing 1-D planar theory [61,62] to represent $\overline{B} < 1$ while seeming to correctly predict $\overline{B} > 1$ data lies in the failure of one-dimensionalized models to adequately account for turbulence and gyration in the cathode-to-anode electron paths. The fully 3D simulations, unlike 1d3v simulations that agree well with 1-D planar theory, can accurately account for this additional behavior, particularly motion in the directions orthogonal to the anode-cathode gap. These alter the force on the electron in the direction across the gap; any increase in the electric field due to binormal, stored current will increase transit time, resulting in a decreased space-charge limit. In fact, as $\overline{B} \to 1$, the electron only asymptotically approaches the anode, which implies infinite transit time and infinite stored current (in the steady state).

The effect of cylindrical geometry is important for designing both conventional and inverted magnetrons. By varying $\bar{a}$ for several fixed values of $\overline{B}$ (including $\overline{B} = 0$), Fig. 13 considers conventional geometry ($\bar{a} < 1$ or $\overline{R}_c < \overline{R}_a$), inverted geometry ($\bar{a} > 1$ or $\overline{R}_c > \overline{R}_a$) and the planar

limit ($\bar{a} \to 1$). For comparison, Fig. 6(a) also considers the Langmuir-Blodgett equation, the first cylindrical solution to SCLE [5]. To more clearly demonstrate the geometric effects, Fig. 13(b) shows normalized results for the same data from Fig. 13(a). Extreme $\bar{a}$ always reduces $\bar{J}_{cr}$, especially for $\bar{B} \approx 1$ – note that the divot for $\bar{B} > 1$ in Fig. 1 occurs for all $\bar{a}$ calculated.

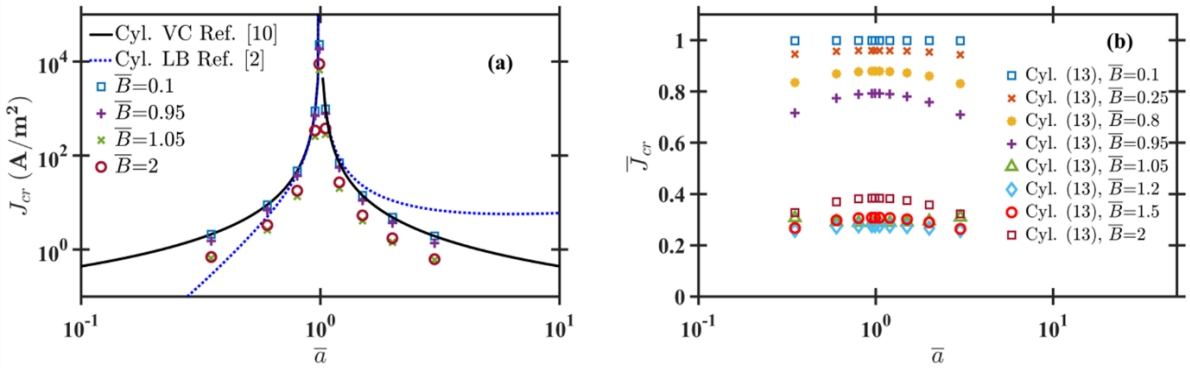


FIG. VII.13. (a) Space-charge limited current density $J_{cr}$ as a function of the ratio of cathode-to-anode radius $\bar{a} = R_c/R_a$ for non-magnetic diodes using variational calculus (VC) [29] and the Langmuir-Blodgett (LB) equation [5] for non-magnetic cylindrical diodes and (57) for several values of dimensionless magnetic field $\bar{B}$ for cylindrical crossed-field diodes. (b) Dimensionless space-charge limited current density $\bar{J}_{cr}$ for a cylindrical crossed-field diode as a function of $\bar{a}$ using (57) for various $\bar{B}$. We include borderline calculations; for $\bar{a} \gg 1$ or $\bar{a} \ll 1$, (57) becomes numerically unstable for $0.95 \lesssim \bar{B} \lesssim 1.05$.

## Incorporating an External Resistance Below the Hull Cutoff

A. M. Darr[G] and **A. L. Garner**, "Modifications of Limiting Current and Magnetic Insulation in a Crossed-Field Diode by a Series Resistor," *IEEE Access* **10**, 60438-60446 (2022).

In this effort, we refined SCLC for crossed-field devices (CFDs) with respect to geometry and additional physical phenomena. We build on our variational calculus approach [29], incorporating the perturbative effect of an external resistor. The injection $J$ required to destabilize laminar flow into the near-Brillouin state was examined using theory and the particle-in-cell (PIC) code XPDP1 [77] for an AC modulation [78], an external resistor to represent dissipation [79], and magnetic field misalignment (tilt) [75], all for $B > B_H$. While these previous assessments focused on $B > B_H$, CFDs operating for $B < B_H$ (and, more precisely, near $B_H$) are also of interest [80].

Rather than finding the stability condition, we focus on elucidating the effect of these perturbations upon SCLC, beginning with an external resistor for $B < B_H$ in this paper. Resistive crossed-field SCLC is important to understand because most field emission devices, including CFDs, use current-limiting shunt resistors to prevent damage to the device in the event of a short [81]. Adding an external series resistor to a crossed-field circuit causes initial transients, including erratic electron trajectories [61,62]; however, the eventual SCLC condition must trend toward a steady-state due to dissipation caused by the resistor. At steady-state, magnetically insulated diodes have net zero current since all charge travels parallel to the cathode in Brillouin or near-Brillouin flow [62]. As such, we restrict our inquiry of resistive crossed-field SCLC to steady-state, non-insulated diodes ($B < B_H$). Implications of high resistances potentially causing the onset of magnetic insulation will be addressed.

We considered several limiting current models. The critical current model, denoted by subscript $c$ throughout, was initially derived for $B < B_H$ from a transit time argument to find the limiting current [61] and later using variational calculus to find the SCLC condition [54]. Both approaches reached the same solution [54]; note, limiting current and SCLC results may differ slightly for magnetically insulated ($B > B_H$) CFDs [76,82]. This model solves the Poisson and Lorentz equations from first principles to maximize current density in the gap. For zero initial velocity $u_0 = 0$ used throughout this paper, the SCLC condition is zero electric field at the cathode [2]. For $B < B_H$, the critical current density $J_c$ can be expressed analytically by (cf. (13)-(15) of Ref. [61])

$$\frac{J_c}{J_{CL}} = \frac{9}{4}\frac{y^2}{(1+y^2)^{3/2}[h(y)]^2}, \tag{60}$$

with $J_{CL}$ is the Child-Langmuir law for SCLC for a one-dimensional, planar diode [83] and $y$ and $h(y)$ described by

$$y = \begin{cases} \frac{1}{h^2}\left[\sin^{-1}(h) - h\sqrt{1-h^2}\right], 0 < y < \frac{\pi}{2} \\ \frac{1}{h^2}\left[\frac{\pi}{2} + \cos^{-1}(h) + h\sqrt{1-h^2}\right], y > \frac{\pi}{2} \end{cases} \tag{61}$$

and

$$y = \frac{(B/B_H)}{\sqrt{1-(B/B_H)^2}}, \tag{62}$$

respectively.

The anode model, subscript $a$, assumes the total current density, including stored current in Brillouin-type flow, cannot exceed $J_{CL}$. This is a reasonable assumption, since for $0 < B < B_H$, $J_c < J_{CL}$ [61]. The current density in $\hat{x}$ is constant due to steady-state continuity $\vec{J} = \rho\vec{v}$, so the highest total current density is at the anode. The emission current density $J_a$ is given by (cf. (22) of Ref. [54])

$$\frac{J_a}{J_{CL}} = \sqrt{1-(B/B_H)^2}. \tag{63}$$

The electric potential model, denoted by subscript $e$, calculates average current density using cathode-to-anode velocity from the Lorentz equation and assuming the electric potential profile is identical to the $B = 0$ case [83]. The emission current density $J_e$ for this model is given by (cf. (24) of Ref. [54])

$$\frac{J_e}{J_{CL}} = \frac{2}{3}\frac{(B/B_H)^3}{\sin^{-1}(B/B_H) - (B/B_H)\sqrt{1-(B/B_H)^2}}. \tag{64}$$

Equations (60)-(64) may be multiplied by an arbitrary emission area $S$ to find the total current $I = JS$. We may then calculate the impedance of the diode gap, $Z_{gap} = V_{gap}/I$. Ohm's law with an external resistor in series is

$$V_{app} = V_{gap} + RI = \left(Z_{gap} + R\right)JS. \tag{65}$$

To supplement these planar models, we may derive an analogous anode model for cylindrical diode impedance. In cylindrical coordinates, SCLC at the cathode for $B = 0$, $J_{SCLC}$, is given by [29]

$$J_{SCLC} = \frac{4\sqrt{2}}{9}\epsilon_0\sqrt{\frac{e}{m}}\frac{V^{3/2}}{R_c^2(|\ln \bar{a}|)^2}, \tag{66}$$

where $\bar{a} \equiv R_c/R_a$ arises from the curvature of the electrodes. Continuity means the ratio of current densities at the cathode and anode is $1/\bar{a}$, since total current is constant [54]. Because this is an anode model, we assume the total current at the anode cannot exceed emitted current, or $|\vec{J}| = J_{SCLC}/\bar{a}$, once cathode emission current density reaches the anode. Using continuity $\vec{J} = \rho\vec{v}$, we note $\rho = v_\theta/J_\theta = v_r/J_r$, where $J_\theta$ is stored current. From (6) and (7b) of Ref. [54], $v_\theta^2/v_r^2 = (B_H/B)^2 - 1$. We define the cylindrical anode model current density $J_{a,cyl}$ as $J_{a,cyl} \equiv J_r$. Converting from anode to cathode by multiplying $J_{a,cyl}$ by $\bar{a}$ yields

$$\frac{J_{a,cyl}}{J_{SCLC}} = \sqrt{1 - (B/B_H)^2}. \tag{67}$$

While (67) appears superficially identical to the planar analogue (63), $B_H$ is defined by the effective gap distance noted earlier ($D_{eff} \equiv 0.5R_a|1 - \bar{a}^2|$) and $J_{SCLC} \neq J_{CL}$ for cylindrical geometries [84]. The corresponding gap impedance $Z_{a,cyl}$ is

$$Z_{a,cyl} = Z_{0,cyl}\frac{1}{\sqrt{1 - \left(B/\tilde{B}_H\right)^2}}, \tag{68}$$

with

$$Z_{0,cyl} = \frac{9m(R_c|\ln \bar{a}|)^2}{4eS\epsilon_0\tilde{B}_H D_{eff}}. \tag{69}$$

A device with constant $B$ and $V_{app}$ may still tune gap impedance using a variable resistor, which reduces $V_{gap}$ according to

$$V_{gap} = \frac{V_{app}}{1 + R/Z_{gap}}, \tag{70}$$

where $Z_{gap}$ depends on model for the current. We can write the gap impedance $Z_c$ associated with $J_c$ as

$$Z_c = Z_0\frac{4}{9}\frac{(1 + y^2)^{3/2}[h(y)]^2}{y^2}, \tag{71}$$

with

$$Z_0 \equiv \frac{9mD}{4eS\epsilon_0 \tilde{B}_H}. \tag{72}$$

The gap impedances $Z_a$ and $Z_e$ are given by

$$Z_a = Z_0 \frac{1}{\sqrt{1-\left(B/\tilde{B}_H\right)^2}} \tag{73}$$

and

$$Z_e = Z_0 \frac{3}{2\left(B/\tilde{B}_H\right)^3}\left[\sin^{-1}\left(B/\tilde{B}_H\right) - \left(B/\tilde{B}_H\right)\sqrt{1-\left(B/\tilde{B}_H\right)^2}\right], \tag{74}$$

respectively.

To assess the possibility of onset of magnetic insulation from resistive effects, we performed planar simulations in XPDP1, a 1d3v (one-dimensional in space, three-dimensional in velocity) particle-in-cell (PIC) simulation code [77]. The simulations used $V_{app} = 12{,}000\,\mathrm{V}$ and $D62.16\,\mathrm{mm}$, giving $B_H = 0.171\,\mathrm{T}$ [76]. Figure 14 shows the velocity in $\hat{x}$, $v_x$, as a function of normalized position $x/D$ at several time steps for $B/B_H = 0.95$. Figure 6(a) shows the steady-state for $R = 0$, while Figs. 14(b)-(f) show the time-progression for $R = 7\,\Omega$. For reference, with $R = 0$, $Z_0 = 12.24\,\Omega$ for this magnetic field. Figure 14(b) shows the first cycloid missing the anode, demonstrating the onset of magnetic insulation. However, not all of the first cycloid misses the anode; subsequent cessation of magnetic insulation truncates the insulated part of the cycloid, which continues to oscillate between the cathode and anode, as shown in Fig. 14(c). This pattern of alternating magnetic insulation and non-insulation continues, with insulated cycloid elements oscillating and deforming inside the gap, as shown in Fig. 14(d). This bimodal pattern continues for many dozens of oscillations, with magnetically insulated segments becoming less frequent and smaller as space-charge from prior, insulated segments builds in the center. Figure 14(e) shows a collapse of the central charge into a turbulent state surrounded by an imperfect ring reminiscent of the first partial cycloid in Fig. 14(b). The final state of this diode is shown in Fig. 14(f), where bimodality has collapsed into a high velocity sheath in $v_x - x$ space surrounding a turbulent, lower velocity core. The number of particles eventually saturates since XPDP1 injects electrons directly, and the behavior oscillates about a single steady-state with characteristics of both insulated and non-insulated current flow, or $B \approx \tilde{B}_H$. Future work may specifically account for the emission mechanisms by using a field or thermionic (or combined thermo-field) emission model to avoid the issues caused by direct injection.

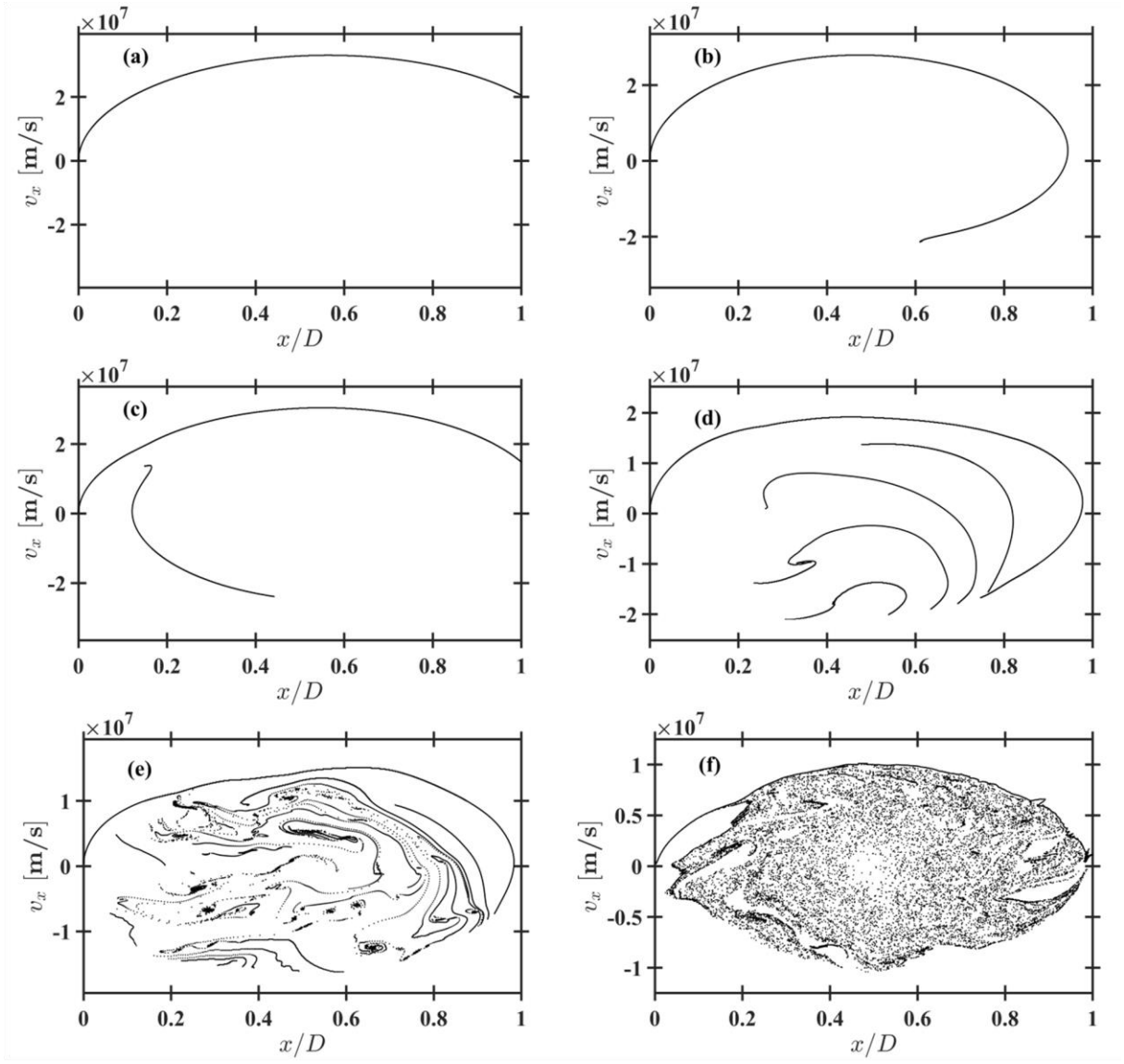


FIG. VII.14. Snapshots of $\hat{\boldsymbol{x}}$ velocity $\boldsymbol{v_x}$ as a function of normalized position $\boldsymbol{x/D}$, where $\boldsymbol{D}$ is the gap distance (2.16 mm), for electrons in XPDP1 [34] for (a) $\boldsymbol{R = 0}$ and (b)-(f) $\boldsymbol{R = 7\ \Omega}$. Applied voltage 12 kV, emission area 14.92 cm$^2$, magnetic field 0.1625 T (95% of Hull cutoff, $\boldsymbol{B_H}$ = 0.171 T). Panel (a) is a stable steady-state; the other snapshots are at specific times: (b) 0.194 ns, (c) 0.287 ns, (d) 1.342 ns, (e) 3.822 ns, and (f) 47.35 ns.

The onset of magnetic insulation and bimodal behavior may be predicted by examining the perturbation of $B/B_H$ to $B/\tilde{B}_H$ for the various impedance models. Figure 15 shows the change from the initial ratio $B/B_H$ to the perturbed ratio $B/\tilde{B}_H$ for several constant values of $R$, compared to the $R = 0$ baseline $B_H = \tilde{B}_H$. In effect, higher $B/\tilde{B}_H$ is caused by a reduction in $V_{gap}$ and $\tilde{B}_H$. The onset of magnetic insulation, and subsequent bimodal oscillations, is indicated whenever $B/\tilde{B}_H$ exceeds unity. This behavior, seen in simulations, does not occur for the anode models in Figs. 15(b) and 15(d), which instead only predict $B/\tilde{B}_H$ *asymptotically approaching* unity. For an

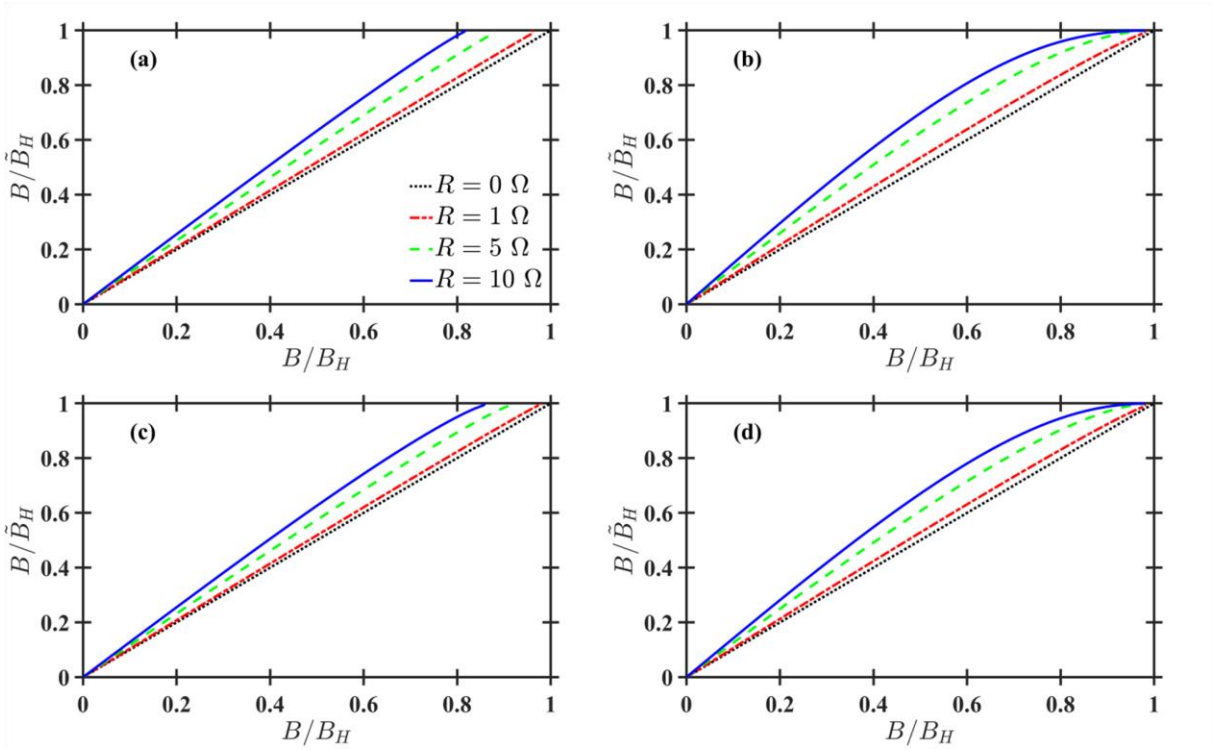


FIG. VII.15. Ratio of magnetic field $\boldsymbol{B}$ to the perturbed Hull cutoff $\widetilde{\boldsymbol{B}}_{\boldsymbol{H}}$ as a function of the ratio of $\boldsymbol{B}$ to the initial Hull cutoff $\boldsymbol{B}_{\boldsymbol{H}}$ for several resistances $\boldsymbol{R}$ for the (a) critical current model, (b) anode model, (c) electric potential model, (d) anode model for cylinders (cathode radius 2.16 mm, anode radius 4.32 mm). Constant diode properties are applied voltage 12 kV, emission area 14.92 cm$^2$, and gap distance 2.16 mm.

alternative perspective, Fig. 16 shows the effect of a variable resistor on a gap. This more clearly shows how increased resistance either brings $B/\tilde{B}_H$ directly to unity (onset of magnetic insulation), or instead only approaches unity for the anode models.

Figure 17 plots critical resistances for onset of magnetic insulation for the critical current model $R_c$ and electric potential model $R_e$ along with XPDP1 simulations. In simulation, we look for two characteristics: minimum $R$ to induce onset of magnetic insulation and minimum $J$ to meet the SCLC condition of zero electric field at the cathode. We define critical $R$ when both these conditions are satisfied simultaneously. As expected, the critical current model agrees well with simulations, though we must again caution that neither represents experimental data appropriately [14].

Finally, Fig. 18 shows the consequences of an external resistor on $J$. The planar models are compared to planar XPDP1 simulations, with $J_{sim}$ found from the SCLC condition as described earlier. The cylindrical anode model has the same trend as the planar anode model, with different $B_H$ and $J_{SCLC}$ normalizations, and as such is omitted. As expected, the simulation results again agree well with the critical current model. For the critical current model, onset of magnetic insulation occurs for $R \approx 12\ \Omega$, which we use as the right-hand termination of the abscissa. The critical current, anode, and electric potential models show reductions in $J$ of 58.2%, 76.1%, and

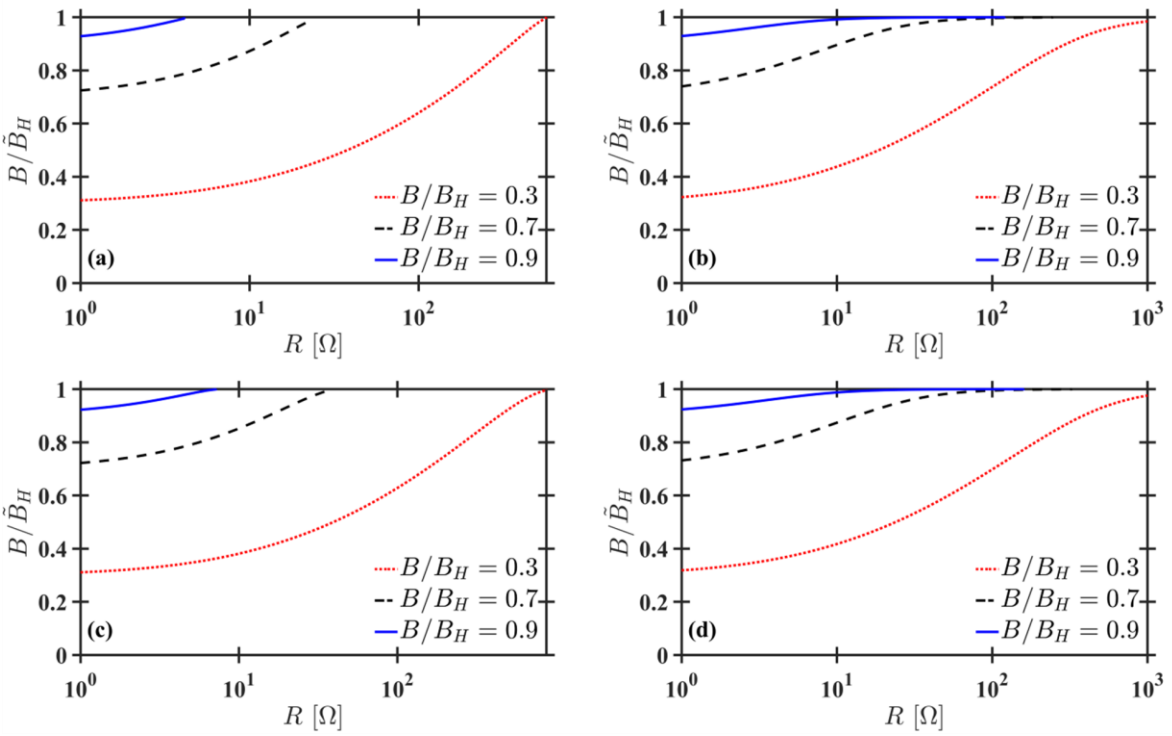


FIG. VII.16. Ratio of magnetic field $\boldsymbol{B}$ to the perturbed Hull cutoff $\widetilde{\boldsymbol{B}}_{\boldsymbol{H}}$ as a function of external resistance $\boldsymbol{R}$ for constant ratio of $\boldsymbol{B}$ to the initial Hull cutoff $\boldsymbol{B}_{\boldsymbol{H}}$ for the (a) critical current model, (b) anode model, (c) electric potential model, (d) anode model for cylinders (cathode radius 2.16 mm, anode radius 4.32 mm). Constant diode properties are applied voltage 12 kV, emission area 14.92 cm$^2$, and gap distance 2.16 mm.

57.9%, respectively, from 0 to 12 Ω. The largest slope in terms of current density loss occurs at low $R$, so even small resistances can significantly lower expected output of a CFD

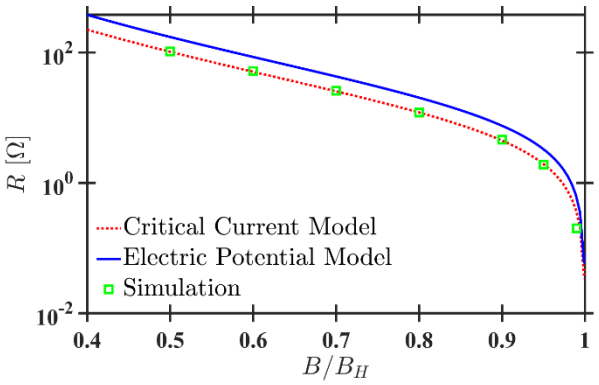


FIG. VII.17 Critical resistance $R$ leading to onset of magnetic insulation as a function of the ratio of $B$ to the non-perturbed Hull cutoff $B_H$ using the critical current model and electric potential models, and from simulations using XPDP. Constant diode properties are applied voltage 12 kV, emission area 14.92 cm$^2$, and gap distance 2.16 mm.

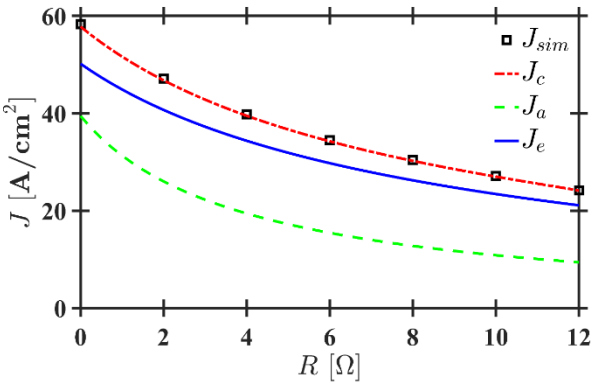


FIG. VII.18. Current density $\boldsymbol{J}$ as a function of resistance $\boldsymbol{R}$ from XPDP1 simulations $\boldsymbol{J_{sim}}$, the critical current model $\boldsymbol{J_c}$, the anode model $\boldsymbol{J_a}$, and the electric potential model $\boldsymbol{J_e}$. Constant diode properties are applied voltage 12 kV, emission area 14.92 cm$^2$, and gap distance 2.16 mm.

# Chapter VII. Publications, Conference Proceedings, and Talks from Project

## BSU

BSU Students:

Graduate Students: Andy Yue, Cesar Segura Del Rio

Undergraduate Students: David Vogel (ECE), Alex Novytskky (ECE), Addie Higgins (ECE), Gerado Herrera (ECE), Isaac Wolstenholme (ECE), Mason Cannon (ECE), Jessica Carlson (MBE), John McClarin (MBE), Liz Gaffney (ECE), Robbie Davis (MBE), Brady Sainz (MBE), Russell Briggs (MBE).

Articles

1. D. Black, R. Harper, P. Ward, J. Davlin, O. Betancourt, D. Plumlee, and J. Browning, “A Cathode Support Structure for use in a Magnetron Oscillator Experiment,” Int J Appl Ceram Technol. 17:2393–2406. (2020)
2. R Bhattacharya, AM Darr, AL Garner, J Browning, “Analysis of Injected Electron Beam Propagation in a Planar Crossed-field Gap”, Appl. Sci., 11(6), 2540. (2021)
3. A. Yue, M. Pearlman, M. Worthington, J. Cipolla, J. Browning, “Particle-in-cell simulation of an industrial magnetron with electron population analysis.” Journal of Vacuum Science & Technology B 1 March; 39 (2): 022201 (2021)
4. A. Yue and J. Browning, "Electron Population Analysis Techniques for Understanding Fundamental Cross-Field Electron Device Physics," in IEEE Transactions on Plasma Science, vol. 50, no. 6, pp. 1775-1780, June (2022)

Conferences

1. R. Bhattacharya et al., "Electron beam Propagation Analysis of a Simple, Planar Crossed-Field Structure," 2022 IEEE International Conference on Plasma Science (ICOPS), Seattle, WA, USA, 2022, pp. 1-2

2. R. Bhattacharya et al., "Gated Field Emitter Arrays for Planar Crossed-Field Device Experiment," 2021 IEEE International Conference on Plasma Science (ICOPS), Lake Tahoe, NV, USA, 2021

3. R. Bhattacharya et al., "High Current Field Emission Arrays for Crossed-Field Device Experiments," 2021 34th International Vacuum Nanoelectronics Conference (IVNC), Lyon, France, 2021, pp. 1-2.

4. Ranajoy Bhattacharya, Adam Darr, A.L. Garner, Jim Browning, "Perturbations in Cross-Field Devices" 47th International Conference on Plasma Science 2020, 6-10 December 2020, Marina Bay Sands, Singapore.

5. A. Yue, J. Browning, M Worthington, and J. Cipolla, "Simulation of an Industrial Magnetron Using Cathode Modulation," IEEE Pulsed Power and Plasma Science Conference, 2020, 6-10 December 2020, Marina Bay Sands, Singapore.

6. A. Yue, J. Browning, M Worthington, and J. Cipolla, "Simulation of an Industrial Magnetron Using Cathode Modulation," International Vacuum Electronics Conference, October 26 - 29, 2020, MONTEREY, CA, USA. "Oral presentation, best student paper award finalist".

7. A. Yue, J. Browning, M Worthington, and J. Cipolla, "Simulation of an Industrial Magnetron Using Cathode Modulation," IEEE Pulsed Power and Plasma Science Conference, 2P10, 25 June 2019. Poster presentation

8. A. Yue, J. Browning, D. Plumlee, M Worthington, J. Cipolla, W. Chren, and T. Akinwande, "An Industrial Magnetron Using Gated Field Emission Arrays for Phase-Control," International Vacuum Nanoelectronics Conference, Cincinnati, OH, 2019

## Purdue

PURDUE Students:

**Graduate Students:** Adam M. Darr (NUCL), N. R. Sree Harsha (NUCL)

**Undergraduate Students:** Jacob M. Halpern (NUCL)

**High School Students:** J. Pan

**Adam M. Darr** – Completed PhD and is a Maxwell Post-Doctoral Fellow at Sandia National Laboratory. 2022 Outstanding Research Award from Nuclear Engineering.

**N. R. Sree Harsha** – Passed qualification examination. Scheduled for Preliminary Exam in April 2023.

**Jacob Halpern** – Completes B. S. in Nuclear Engineering May 2023. Accepted to PhD programs at Columbia, Princeton, and Stanford. Awarded Fulbright, NSF Graduate Fellowship, and Department of Energy Computational Science Graduate Fellowship (DOE CSGF).

**J. Pan** – Currently a First-Year undergraduate student in Nuclear Engineering at UC Berkeley.

REFEREED JOURNAL ARTICLES

1. **[FEATURED ARTICLE]** A. M. Darr[G] and **A. L. Garner**, "A Coordinate System Invariant Formulation for Space-Charge Limited Current in Vacuum," *Applied Physics Letters* **115**, 054101 (2019). [Selected for Featured Article: https://doi.org/10.1063/1.5121645]

2. **[INVITED PERSPECTIVE] A. L. Garner**, G. Meng, Y. Fu, A. M. Loveless[G,P], R. S. Brayfield II[G], and A. M. Darr[G], "Transitions between electron emission and gas breakdown mechanisms across length and pressure scales," *Journal of Applied Physics* **128**, 210903 (2020).

3. **[INVITED PERSPECTIVE, FEATURED]** P. Zhang, Y. S. Ang, **A. L. Garner**, Á. Valfells, J. W. Luginsland, and L. K. Ang, "Space-charge limited current in nanodiodes: Ballistic, Collisional and Dynamical Effects," *Journal of Applied Physics* **129**, 100902 (2021).

4. N. R. Sree Harsha[G] and **A. L. Garner**, "Applying Conformal Mapping to Derive Analytical Solutions of Space-Charge-Limited Current Density for Various Geometries," *IEEE Transactions on Electron Devices* **68**, 264-270 (2021).

5. A. M. Darr[G], N. R. Sree Harsha[G], and **A. L. Garner**, "Response to "Comment on 'A coordinate system invariant formulation for space-charge limited current in vacuum" [Appl. Phys. Lett. 118, 266101 (2021)]," *Applied Physics Letters* **118**, 266102 (2021).

6. A. M. Darr[G], R. Bhattacharya[P], J. Browning, and **A. L. Garner**, "Space-Charge Limited Current in Planar and Cylindrical Crossed-Field Diodes using Variational Calculus," *Physics of Plasmas* **28**, 082110 (2021).

7. N. R. Sree Harsha[G] and **A. L. Garner**, "Analytic Solutions for Space-Charge-Limited Current Density from a Sharp Tip," *IEEE Transactions on Electron Devices* **68**, 6525-6531 (2021).

8. A. M. Darr[G], N. R. Sree Harsha[G], and **A. L. Garner**, "Response to Comment on "A coordinate system invariant formulation for space-charge limited current in vacuum" [APL 119, 206101 (2021)]," *Applied Physics Letters* **119**, 206102 (2021).

9. **[FEATURED]** N. R. Sree Harsha[G], M. Pearlman[P], J. Browning, and **A. L. Garner**, "A multi-dimensional Child-Langmuir law for any diode geometry," *Physics of Plasmas* **28**, 122103 (2021).

10. **[INVITED] A. L. Garner**, A. M. Darr[G], and N. R. Sree Harsha[G], "A Tutorial on Calculating Space-Charge Limited Current Density for General Geometries and Multiple Dimensions," *IEEE Transactions on Plasma Science* **50**, 2528-2540 (2022).

11. A. M. Darr[G] and **A. L. Garner**, "Modifications of Limiting Current and Magnetic Insulation in a Crossed-Field Diode by a Series Resistor," *IEEE Access* **10**, 60438-60446 (2022).

12. J. M. Halpern[U], A. M. Darr[G], N. R. Sree Harsha[G], and **A. L. Garner**, "A coordinate system invariant formulation for space-charge limited current with nonzero injection velocity," *Plasma Sources Science and Technology* **31**, 095002 (2022).

13. N. R. Sree Harsha[G], J. M. Halpern[U], A. M. Darr[G], and **A. L. Garner**, "Space-charge-limited current density for nonplanar diodes with monoenergetic emission using Lie-point symmetries," *Physical Review E* **106**, L063201 (2022).

CONFERENCE PAPERS

14. N. R. Sree Harsha[G] and **A. L. Garner**, "Analytical Solution for Space Charge Limited Current Emission from a Sharp Tip Using Variational Methods," IEEE International Vacuum Electronics Conference, P8.22, 22 October 2020, pp. 395-396.

CONFERENCE ORAL PRESENTATIONS

15. *N. R. Sree Harsha*[G], A. M. Darr[G], J. M. Halpern[U], **A. L. Garner**, "Novel techniques for deriving the space-charge limited current for nonplanar diodes," 2022 IEEE International Power Modulator Conference (IPMHVC), Knoxville, TN, Analytical Methods Section, 22 June 2022.

16. *N. R. Sree Harsha*[G], J. M. Halpern[U], A. M. Darr[G], and **A. L. Garner**, "Using Lie symmetries to derive space-charge-limited current in non-planar diodes with nonzero injection velocity," IEEE International Conference on Plasma Science, Seattle, WA, MO 4.1-4, 4.1 – 1.1, 26 May 2022.

17. *J. M. Halpern*[U], A. M. Darr[G], N. R. Sree Harsha[G], and **A. L. Garner**, "Space-charge-limited current in non-planar diodes with nonzero injection velocity," IEEE International Conference on Plasma Science, Seattle, WA, MO 4.1-3, 4.1 – 1.1, 26 May 2022.

18. *A. M. Darr*[G] and **A. L. Garner**, "Resistor effects on non- and semi-magnetically insulated crossed-field devices," IEEE International Conference on Plasma Science, Seattle, WA, AO 3.4-2, 3. 4– 2.2/2.3, 25 May 2022.

19. *R. Bhattacharya*, J. McClarin, B. Sainz, A. Yue, I. Wolstenholme, M. Cannon, G. Herrera, L. Gaffney, A. M. Darr, G. Rughoobur, W. Chern, **A. L. Garner**, A. I. Akinwande, and J. Browning," IEEE International Conference on Plasma Science, Seattle, WA, MO 3.5-2, 3. 5 – 6.2/6.3, 25 May 2022.

20. *N. R. Sree Harsha*[G], A. Darr[G], and **A. Garner**, "Space-charge limited current: Extensions to non-planar, multidimensional, and crossed-field diodes," 63rd Annual Meeting of the American Physical Society Division of Plasma Physics, ZO05.00012, Virtual 12 November 2021.

21. **[INVITED PLENARY]** A. Garner, "Diode physics: From Child-Langmuir to Paschen's law," 2021 IEEE International Conference on Plasma Science, Plenary 8, Virtual 15 September 2021.

22. *J. Halpern*[U], A. Darr[G], N. R. Sree Harsha[G], and **A. Garner**, "Space-charge-limited current for nonzero electron injection velocity in non-planar diodes," 2021 IEEE International Conference on Plasma Science, 7O-B-05, Virtual 15 September 2021.

23. *N. R. Sree Harsha*[G] and **A. Garner**[G], "Multi-dimensional space-charge limited current using variational calculus and vacuum capacitance," 2021 IEEE International Conference on Plasma Science, 7O-B-03, Virtual 15 September 2021.

24. A. Darr[G], J. Pan[H], R. Bhattacharya[P], J. Browning, and **A. Garner**, "Space-charge limited current for a nonplanar crossed-field diode," 2021 IEEE International Conference on Plasma Science, 7O-B-02, Virtual 15 September 2021.

25. *A. Darr*[G], Sree Harsha N R[G], and **A. Garner**, "Space-charge Limited Emission in Crossed Field Diodes using Variational Calculus," 62nd Annual Meeting of the American Physical Society Division of Plasma Physics, BO03.00013, 10 November 2020.

26. *A. Darr*[G] and **A. Garner**, "Space-charge limited current calculation using the minimum energy principle," American Physical Society Division of Plasma Physics, Bull. Am. Phys. Soc., Vol. 64, JO4.00007 (2019).

27. *A. Darr*[G] and **A. Garner**, "A Coordinate Invariant Theory for Space Charge Limited Emission using Variational Calculus," IEEE Pulsed Power and Plasma Science Conference, 10A5, 28 June 2019.

POSTER PRESENTATIONS

28. *J. Halpern*[U], A. Darr[G], and **A. Garner**, "Coordinate System Invariant Space Charge Limited Current for General Initial Velocity," 62nd Annual Meeting of the American Physical Society Division of Plasma Physics, JP13.00098, 10 November 2020.

29. *N. R. Sree Harsha*[G] and **A. L. Garner**, "Analytical Solution for Space Charge Limited Current Emission from a Sharp Tip Using Variational Methods," IEEE International Vacuum Electronics Conference, P8.22, 22 October 2020.

INVITED SEMINARS OR COLLOQUIA

30. ***A. L. Garner***, "Space-charge limited current: Extending beyond the Child-Langmuir law," Lawrence Livermore National Laboratory, Livermore, CA, 12 December 2022.

31. ***A. L. Garner***, "Extending Space-Charge Limited Current Theories to Nonplanar and Multidimensional Geometries," Science, Mathematics and Technology Online Research Seminar, Singapore University of Technology and Design (SUTD), Singapore, 24 February 2022.

32. ***A. L. Garner***, "Directed Energy: From Source to Molecular Interactions," School of Nuclear Engineering, Purdue University, West Lafayette, IN 10 March 2021 (Delivered remotely due to COVID-19).

33. ***A. L. Garner***, "Re-envisioning Electron Emission Physics," Sandia National Laboratories, Albuquerque, NM, 17 August 2020. (Delivered remotely due to COVID-19).

34. ***A. L. Garner***, "Unified Electron Emission Theory and Experimental Validation," Department of Electrical and Computer Engineering, Oak Ridge National Laboratory, Oak Ridge, TN, 03 March 2020.

35. ***A. L. Garner***, "Unified Electron Emission Theory and Experimental Validation," Department of Electrical and Computer Engineering, University of New Mexico, Albuquerque, NM, 06 December 2019.

36. ***A. L. Garner***, "Theoretical and Experimental Unification of Electron Emission Mechanisms," Department of Electrical and Computer Engineering, Boise State University, Boise, ID, 04 December 2019.

37. ***A. L. Garner***, "Electron Emission and Gas Breakdown from Quantum to Classical Lengths," Plasma Seminar Series, University of Washington, Seattle, WA, 02 December 2019.

38. ***A. L. Garner***, "Progress Toward a Universal, Unified Electron Emission Theory," Air Force Research Laboratory, Air Force Research Laboratory, Albuquerque, NM, 11 July 2019.

39. ***A. L. Garner***, "Unification of Electron Emission and Gas Breakdown Mechanisms: Experiment and Theory," Sandia National Laboratories, Albuquerque, NM, 10 July 2019.

MINI-COURSES AND SPECIAL PRESENTATIONS:

40. ***A. L. Garner***, "Unification of Electron Emission and Breakdown Mechanisms: Experiments and Theory," Minicourse, 2022 IEEE International Power Modulator and High Voltage Conference (IPMHVC), Knoxville, TN, 23 June 2022.

# Chapter VI. References


1. R Bhattacharya, AM Darr, AL Garner, J Browning, "Analysis of Injected Electron Beam Propagation in a Planar Crossed-field Gap", Appl. Sci. 2021, 11(6), 2540.
2 I. Langmuir, The effect of space charge and residual gases on thermionic currents in high vacuum, Phys. Rev. **2**, 450-486 (1913).
5. Y. Y. Lau, Simple theory for the two-dimensional Child-Langmuir law, Phys. Rev. Lett. **87**, 278301 (2001).
6. Sean R. Koebleya and Ronald A. Outlawb, "Degassing a vacuum system with in-situ UV radiation", Journal of Vacuum Science & Technology A 30, 060601 (2012)
7. R.H. Fowler and L. Nordheim, "Electron emission in intense electric fields", Proceedings of the Royal Society of London. Series A, Containing Papers of a Mathematical and Physical Character **119**, 173 (1928).
8. P. L. Walraven, Test of Langmuir's three halves power law, deviations due to $\beta^2$-factor and secondary emission, Appl. Sci. Res. B **3**, 393-399 (1953).
9. S. Mahalingam, C. Nieter, J. Loverich, D. Smithe and P. Stoltz, Space charge limited currents calculations in coaxial cylindrical didoes using particle-in-cell simulations, Open Plasma Phys. J. **2**, 63-69 (2009).

10. I. Langmuir and K. Blodgett, Currents limited by space charge between coaxial cylinders, Phys. Rev. **22**, 347-356 (1923).
11. I. Langmuir and K. Blodgett, Currents limited by space charge between concentric spheres, Phys. Rev. **24**, 49-59 (1924).
12. L. Page and N. I. Adams, Diode space charge for any initial velocity and current, Phys. Rev. **76**, 381-388 (1949).
13. I. Itzkan, Solutions of the equations of space charge flow for radial flow between concentric spherical electrodes, J. Appl. Phys. **31**, 652-655 (1960).
14. J. H. Porter, W. Franzen and R. S. Wenstrup, A new analysis of space-charge-limited emission between concentric spheres and concentric cylinders, J. Appl. Phys. **43**, 344-354 (1972).
15. L. H. Germer, The distribution of initial velocities among thermionic electrons, Phys. Rev. **25**, 795-807 (1925).
16. D. Lai, M. Qiu, Q. Xu and Z. Huang, Space-charge-limited currents for cathodes with electric field enhanced geometry, Phys. Plasmas **23**, 083104 (2016).
17. J. W. Luginsland, Y. Y. Lau, and R. M. Gilgenbach, Two-dimensional Child-Langmuir law, Phys. Rev. Lett. **77**, 4668 (1996).
18. M. Zubair and L. K. Ang, Fractional-dimensional Child-Langmuir law for a rough cathode, Phys. Plasmas **23**, 072118 (2016).
19. W. S. Koh, L. K. Ang, and T. J. T. Kwan, Three-dimensional Child–Langmuir law for uniform hot electron emission, Phys. Plasmas **12**, 053107 (2005).
20. I. M. Rittersedorf, P. F. Ottinger, R. J. Allen and J. W. Schumer, Current density scaling expressions for a bipolar space-charge-limited cylindrical diode, IEEE Trans. Plasma Sci. **43**, 3626-3636 (2015).
21. L. Page and N. I. Adams, Space charge in cylindrical magnetron, Phys. Rev. **69**, 494-500 (1946).
22. S. B. Swanekamp, R. J. Commisso, G. Cooperstein, P. F. Ottinger and J. W. Schumer, Particle-in-cell simulations of high-power cylindrical electron beam diodes, Phys. Plasmas **7**, 5214-5222 (2000).
23. P. Y. Chen, T. C. Cheng, J. H Tsai and Y. L. Shao, Space charge effects in field emission nanodevices, Nanotechnol. **20**, 405202 (2009).
24. L. Oksuz, Analytical solution of space charge limited current for spherical and cylindrical objects, Appl. Phys. Lett. **88**, 181502 (2006).
25. R. Kumar and D. Biswas, Electromagnetic power loss in open coaxial diodes and the Langmuir-Blodgett law, Phys. Plasmas **17**, 104506 (2010).
26. L. Page and N. I. Adams, Space charge between coaxial cylinders, Phys. Rev. **68**, 126-129 (1945).
27. R. Torres-Cordoba and E. Martinez-Garcia, Analytical and exact solutions of the spherical and cylindrical diodes of Langmuir-Blodgett law, Phys. Plasmas **24**, 103113 (2017).
28. C. B. Wheeler, The approach to space charge limited current flow between coaxial cylinders, J. Phys. A: Math. Gen. **8**, 555-559 (1975).
29. C. B. Wheeler, The approach to space charge limited current flow between concentric spheres, J. Phys. A: Math. Gen. **8**, 1159-1163 (1975).
30. C. B. Wheeler, Space charge limited current flow between coaxial cylinders at potentials up to 15 MV, J. Phys. A: Math. Gen. **10**, 631-636 (1977).
31. C. B. Wheeler, Space charge limited current flow between concentric spheres at potentials up to 15 MV, J. Phys. A: Math. Gen. **10**, 1645-1649 (1977).

32. L. Gold, Transit time and space-charge for the cylindrical diode, Int. J. Electr. **3**, 567-572 (1957).
33. Y. B. Zhu, P. Zhang, A. Valfells, L. K. Ang and Y. Y. Lau, Novel scaling laws for the Langmuir-Blodgett solutions in cylindrical and spherical diodes, Phys. Rev. Lett. **110**, 265007 (2013).
34. X. Chen, J. Dickens, L. L. Hatfield, E.-H. Choi and M. Kristiansen, Approximate analytical solutions for the space-charge-limited current in one-dimensional and two-dimensional cylindrical diodes, Phys. Plasmas **11**, 3278-3283 (2004).
35. D. Anderson and M. Desaix, Introduction to direct variational and moment methods and an application to the Child-Langmuir law, Eur. J. Phys. **36**, 065032 (2015).
36. A. Rokhlenko, Minimum current principle and variational method in theory of space charge limited flow, J. Appl. Phys. **118**, 153303 (2015).
37. B. van Brunt, *The Calculus of Variations* (Universitext, New York, 2004).
38. M. Zubair and L. K. Ang, Fractional-dimensional Child-Langmuir law for a rough cathode, Phys. Plasmas **23**, 072118 (2016).
39. K. D. Bergeron, Equivalent circuit approach to long magnetically insulated transmission lines, J. Appl. Phys. **48**, 3065-3069 (1977).
40. Y. Y. Lau, Effects of cathode surface roughness on the quality of electron beams, J. Appl. Phys. **61**, 36-44 (1987).
41. R. W. Lemke, S. E. Calico, and M. C. Clark, Investigation of a load-limited, magnetically insulated transmission line oscillator (MILO), IEEE Trans. Plasma Sci. **25**, 364-374 (1997).
42. S. M. Rossnagel and H. R. Kaufman, Charge transport in magnetrons, J. Vacuum Sci. Technol. A **5**, 2276 (1987).
43. Y. Y. Lau, D. Chernin, D. G. Colombant, and P.-T. Ho, Quantum extension of Child-Langmuir law, Phys. Rev. Lett. **66**, 1446-1449 (1991).
44. L. K. Ang, T. J. T. Kwan, and Y. Y. Lau, New scaling of Child-Langmuir law in the quantum regime, Phys. Rev. Lett. **91**, 208303 (2003).
45. L. K. Ang, Y. Y. Lau, and T. J. T. Kwan, Simple derivation of quantum scaling in Child-Langmuir law, IEEE Trans. Plasma Sci. **32**, 410-412 (2004).
46. L. K. Ang and P. Zhang, Ultrashort-pulse Child-Langmuir law in the quantum and relativistic regimes, Phys. Rev. Lett. **98**, 164802 (2007).
47. E. W. V. Acton, The space-charge limited flow of charged particles in planar, cylindrical and spherical diodes at relativistic velocities, Int. J. Elect. **3**, 203-210 (1957).
48. A. D. Greenwood, J. F. Hammond, P. Zhang, and Y. Y. Lau, On relativistic space charge limited current in planar, cylindrical, and spherical diodes, Phys. Plasmas **23**, 072101 (2016).
49. Y. L. Liu, S. H. Chen, W. S. Koh, and L. K. Ang, Two-dimensional relativistic space charge limited current flow in the drift space, Phys. Plasmas **21**, 043101 (2014).
50. M. Mitsunaga and R. G. Brewer, Generalized perturbation theory of coherent optical emission, Phys. Rev. A **32**, 1605-1613 (1985).
51. P. Hommelhoff, Y. Sortais, A. Aghajani-Talesh, and M. A. Kasevich, Field emission tip as a nanometer source of free electron femtosecond pulses, Phys. Rev. Lett. **96**, 077401 (2006).
52. Y. Y. Lau, Y. Liu, and R. K. Parker, Electron emission: From the Fowler-Nordheim relation to the Child-Langmuir law, Phys. Plasmas **1**, 2082 (1994).
53. A. M. Darr, A. M. Loveless, and A. L. Garner, Unification of field emission and space charge limited emission with collisions, Appl. Phys. Lett. 114, 014103 (2019).